# POLITECNICO DI TORINO

**Master's Degree in Mechanical Engineering**


**Master's Degree Thesis**

# Reactor Design and CFD simulation of a bio-electrical system


**Supervisors**

**Prof. Eugenio BRUSA**

**MER Jan VAN HERLE**

**Prof. Massimo SANTARELLI**

**Candidate**

**Matteo ARDUINI**


**October 2022**

# Acknowledgements

*Vorrei ringraziare chi mi ha sempre supportato in ogni fase di questo bellissimo percorso universitario: la mia famiglia, i miei amici, i miei colleghi*

# Table of Contents

# List of Tables

# List of Figures

# Glossary

**AD** Anaerobic Digester

**BC** Boundary Condition

**BES** Bio-Electrochemical System

**CFD** Computational Fluid Dynamics

**COD** Chemical Oxygen Demand

**EC** Electrolysis Cell

**FC** Fuel Cell

**FVM** Finite Volume Method

**GCI** Grid Convergence Index

**HRT** Hydraulic Retention Time

**MEC** Microbial Electrolysis Cell

**MES** Microbial Electrolysis System

**MFC** Microbial Fuel Cell

**SS** Stainless Steel

**WW** Wastewater

# Nomenclature

### Greek symbols

| | |
|---|---|
| $\chi$ | Surface tension coefficient |
| $\eta$ | Efficiency |
| $\mu$ | Dynamic Viscosity |
| $\rho$ | Density |
| $\sigma$ | Electrical Conductivity |
| $\varepsilon$ | Porosity |

### Physics constants

| | |
|---|---|
| R | Universal Gas constant |
| $\dot{m}$ | Mass flow rate |
| $\dot{V}$ | Volume flow rate |
| $C$ | Concentration |
| $c_p$ | Specific heat capacity |
| $F$ | Faraday constant, 9.6487 x $10^7$ C $kmol^{-1}$ |
| $I$ | Current |
| $K$ | Permeability |

$k$ Heat transfer coefficient

$p$ Pressure

$R$ Volumetric current

$S$ Source term

$s$ Volume fraction

$V$ Volume

$v$ Velocity

$Y$ Mass fraction

**Subscripts and superscripts**

$CH_3COO^-$ Acetate

$CH_4$ Methane

$CO_2$ Carbon Dioxide

WW Wastewater

$an$ Anode region

$cat$ Cathode region

$CE$ Coulombic Efficiency

$eff$ Effective

$g$ Gas phase

$l$ Liquid phase

$m$ Mixture

# Chapter 1

# Introduction

This Master's Thesis focuses on the first steps in the simulation and optimization of a new bio-electrical reactor used for producing biomethane from organic waste waters, which may come from: sewage, cheese factories, breweries, distilleries. The work presented here deals with the initial development of a CFD model for a biomethane-producing electrochemical reactor, and its validation with respect to experimental data.

The model will be later adopted to layout and predict the performance of cylindrical cells for different anode and cathode geometries, positioning, and morphology (porosity). Outputs of interest include fluid velocity and pressure, current density, methane production rate, liquid-gas separation, and utilization factor of organic contaminants (model based on low concentrations of acetates).

This work places itself in the broader research objective of the EPFL Laboratory GEM – Group of Energy Materials, led by Jan Van Herle, which is to realize the construction of a novel bioelectrical reactor to produce highly upgraded biogas, with methane content over 90%, from wastewaters and other CO2 sources, ideally ready for gas grid injection. Bio-methane production is supported by new evidence about Bio-electrical systems, able to consume wastewaters organics by oxidation, and form methane by reduction of the carbon dioxide. Many renewable applications may be based on this technology, which exploits microbial catalyzation to lower

the energy demand of the process, which allows on one side to lower the Chemical Oxygen Demand of the wastewaters, while collecting the produced bio-methane as well. The scale-up of this technology and its marketability are now becoming to be addressed, by designing and testing bigger reactors, which may benefit from theoretical models and simulations in order to be optimized.

Therefore, the topics investigated in this work may be categorized in one of the project's Technical work packages, focusing on CFD simulations, CAD design, and material selection.

The work developed in this thesis has been structured as follows:

- Chapter 2 focuses on the theory supporting the Microbial Electrolysis Cells for the production of bio-methane. Studies about successful electromethanogenesis are presented, pointing out the working principles of such reactors. The different electrochemical methane pathways are listed, focusing on the appealing $CO_2$ Reduction mechanism, which is promising considering the higher methane output rates that have been experimentally obtained. This mechanism has been already investigated as a stand-alone methane production technique, as in Cheng et al. [1], or integrated with a conventional anaerobic digester by being placed downstream to collect its effluent [2]. Furthermore, in the same paper by Nelabhotla and Dinamarca working conditions such as electrodes potential and pH have been optimized. However, tested prototypes still refer to small scale reactors operating at very low flow rates. The pilot design of a large scale reactor is presented [3], even if its whole output rates are simply assumed to be the scaled from another experimental work, 5 orders of magnitude smaller. Lastly, possible applications of this technology are presented.

- Chapter 3 reports basic theory elements about Computational Fluid Dynamics, and more in general presents the involved numerical methods, mainly the Finite Volume Method. Furthermore, CFD studies about fuel and electrolysis cells are presented, whose governing equations will support the model treated

here. More specifically, a study on anaerobic co-digestion has been selected as the reference for the Grid Convergence Study that will be performed on the mesh being developed for the model.

- Chapter 4 is dedicated to the presentation of the Reference Study, whose experimental data have been used to perform the model validation. The study by Rader and Logan [4] features a single chamber membrane-less continuous flow reactor, equipped with eight electrodes pairs, working with an horizontal liquid flow and an upward gas motion. Influent substrate contains acetate, while the output converged to only methane gas after a two-weeks period. Current values measured at the electron pairs have been reported as well.

- Chapter 5 is focused on the development of the model for a Microbial Electrolysis Cell, by presenting the two key objectives, along with the assumptions made and the fundamental governing equations, describing mathematically the physical phenomena taking place. In order of appearance, the geometry of reactor is presented, followed by the developed mesh grid. Governing equations and electrochemical assumptions are followed by a section about the multiple phases present in the reactor nature, which concludes the chapter.

- Chapter 6 is dedicated to the presentation of the numerical results, obtained by running the CFD model. The parameters of interest are compared to the experimental data provided by Rader and Logan, to later assess whether the model may be considered validated. Furthermore, additional numerical data is presented, and compared with the theoretical values computed from the Reference Study available data.

- Chapter 7 contains the conclusion of this thesis: it is argued that a partial validation of the model has been reached, specifically about the electrochemical phenomena present inside the reactor, with errors below 10%.. On the other side, the simulation of multiple phases, i.e. liquid and gaseous, was not entirely successful, as it did not lead to a stable convergence of the numerical solution.

The takeaways from this study are listed here, along with possible future improvements to continue the research on this sensible topic.

# Chapter 2

# Theory of Microbial Electrolysis Cells

In the attempt of presenting the working principles relative to the electrochemical production of methane, starting from organic molecules such as acetic acid, the work by Blasco-Gómez et al. [5] represents a crucial contribution. In their work, the technological developments made in this field over the years are presented, while listing the electrochemical mechanisms that may take place in BES. Therefore, this work will serve as the main reference in this Chapter, along with other studies that will be presented later.

As reported in their study [5], the first use of the word "electromethanogenesis" appeared in 2009 in a study by Cheng et al. [1], referring to the conversion pathway of carbon dioxide to methane by means of a single Archaeon (Methanobacterium palustre).

Furthermore, systems designed for the production of hydrogen or methane gas by means of the aforementioned mechanism may be named "Microbial Electrolysis Cells" (MEC). Hydrogen is included in the desired products of these reactors, since many researches first focused on its production, dealing with methane as an undesired side effect to be eliminated, as in Sasaki et al. [6] and Clauwaert and Verstraete [7]. However, rather than focusing on the elimination of methanogens,

later studies intensified the research on the possibility to produce and/or upgrade bio-methane. Finally, the present possible application will be addressed in Section 2.6.

## 2.1 Electromethanogenesis Pathways

According to Blasco-Gómez et al. [5], the variety of reactions occurring at the bio-cathode of MECs for methane production may be classified in three main methanogenesis pathways.

**Acetoclastic** The acetoclastic pathway is usually the mainstream route taking place in the anaerobic digestion of organic wastes, such as for industrial waster, dairy, wastewaters, manure. Studies, such as the one by Kurade et al. [8], suggest that the dominant microbial population in such working conditions is the *Archea* of the genus *Methanosarcina*. Equation 2.1 highlights how the acetoclastic methanogens use acetate as electron acceptor:

$$CH_3COOH \rightarrow CH_4 + CO_2 \tag{2.1}$$

**Methylotrophic** Contrarily to acetoclastic methanogens, methylotrophic ones use methanol or methylamines as electron acceptor, according to Mobilian and Craft [9].

**$CO_2$ Reduction** As stated by Blasco-Gómez et al. [5], this is considered the major pathway driving the methane production in BES. Hydrogenotropic methanogens, such as the *Methanobacterium palustre* from the study of Cheng et al. [1], use $H_2$ and $CO_2$ to carry out methanogenesis [9], and may follow two different routes in order to transfer electrones, which will presented later in Section 2.1.1.

However, when working with mixed cultures it becomes much harder to trace back the responsible for such methane production, due to the complexity of microbial population. As a matter of fact, if an electromethanogensis reactor exploiting

$CO_2$ reduction is placed downstream of another digestion process, acetoclastic methanogens may reach the chamber and of the reactor and populate it. In light of the above, the efforts present in multiple studies to focus only on $CO_2$ reduction become understandable. For example in the work by Nelabhotla and Dinamarca, the influent wastewaters from a municipal plant had been autoclaved, in order to "ensure all the biomethane produced is from the biofilm present on the carbon felt cathodes and not from suspended biomass" [2]. This procedure allowed to obtain a deeper understanding of the phenomenon, estimating that hydrogenotropic methanogens in a MEC are able to increase the methane output by roughly 15%, compared to "open-circuit" acetoclastic digestion. The model developed in this work will heavily rely on this estimation.

Analogously, Cheng et al. [1] conduced experiments in a two-chamber MEC, successfully verifying the presence of electromethanogenesis in absence of acetate, therefore without the possibility to follow the acetoclastic pathway.

### 2.1.1 $CO_2$ Reduction: Extracellular Electron Transfer

**Direct** As stated by Van Eerten-Jansen et al. [10], with Direct electron transfer, electrons travelling to the cathode are taken directly and used to reduce carbon dioxide to produce methane:

$$CO_2 + 8H^+ + 8e^- = CH_4 + 2H_2O \quad (E_{cat} = -0.24\,\text{V vs. NHE}) \tag{2.2}$$

**Indirect** On the contrary, with indirect electron, intermediate production of hydrogen occurs, which is later used together with $CO_2$ for methane formation:

$$2H^+ + 2e^- = H_2 \quad (E_{cat} = -0.41\,\text{V vs. NHE}) \tag{2.3}$$

$$CO_2 + H_2 = CH_4 + 2H_2O \tag{2.4}$$

Van Eerten-Jansen et al. [10] also point out that "Methane production via direct extracellular electron transfer is considered the most energy-efficient process, as the standard potential of hydrogen production via indirect extracellular electron

transfer is lower than that of methane production via direct extracellular electron transfer"

## 2.2 MEC Electrochemistry

### 2.2.1 Redox Half-reactions

After having presented the available electrochemical methanogenic pathways, in this Section more focus is given to the half reactions designed to take place in the new MEC reactor which will be based on the model being developed in this thesis work. Therefore, reactions at anode and cathode are investigated, to match the initial design purpose of consuming acetate by oxidizing it into carbon dioxide, which will be reduced at the cathode to form methane, as stated by Equation 2.5.

$$CH_3COO^- + H_2O = HCO_3^- + CH_4 \tag{2.5}$$

While the complete redox that is designed to take place in reactor is reported in Equation 2.5, the relative half reactions will addressed in the next Sections, following the work by Bhattacharya et al. [11].

#### Anode

In several MECs the role of the anode is to provide electrons to the bio-cathode. This could be done by oxidizing water as in the case of the work by Van Eerten-Jansen et al. [10]. However, by designing a bio-anode populated by *Geobacter* [12], organic molecules such as acetic acid may be oxidized with a two-fold purpose. On one side, acetic acid originated in other industrial applications may be disposed correctly by electrochemically consuming it, instead of realising it in the environment. Secondarily, this allows to provide both $CO_2$ and electrons to the bio-cathode, by travelling in the electrolyte and by conducting materials (wires), respectively.

Also the work of Cheng et al. has demonstrated high efficiencies above 80%, by including in the system an "exoelectrogenic biofilm on the anode, growing on

acetate in a single-chamber MEC" [1].

Therefore, the half reaction of acetate oxidation is here reported:

$$CH_3COO^- + 3H_2O = CO_2 + HCO_3^- + 8H^+ + 8e^- \quad (E_{an} = 0.29\,\text{V vs. NHE}) \tag{2.6}$$

### Cathode

The designed half reaction for the bio-cathode would be direct extracellular electron transfer, catalyzed by hydrogenotropic methanogens, i.e. 2.2. As previously stated, Van Eerten-Jansen et al. identify this as more efficient than indirect electron transfer [10]. However, the presence of acetoclastic methanogens will not be considered a problematic side effect, but rather a positive addition, since the new reactor designed in this work has the objective to consume the most possible organic load contained in reject WW, already passed through a treatment plant and otherwise to be released in the environment. Therefore the presence of acetoclastic methanogens, for instance acquired from an upstream AD is welcomed, as it investigated in paper by Nelabhotla and Dinamarca [2].

The work of Siegert et al. [12] focused on investigating MEC archeal communities, to see if convergence to a specific genus was analogous as for geobacter in anodes. Results showed *Methanobacterium* and *Methanobrevibacter* Furthermore, Blasco-Gómez et al. [5] reported how other studies proved the ability of *Methanosarcina* to produce methane by direct electron transfer.

Lastly, experimantal data from Cheng et al. [1] pointed out that their biocathode designed for $CO_2$ reduction was dominated by *Methanobacterium palustre*, achieving important a notable increase in current densities. As it will be explained later in Section 2.3.1, current densities are crucial to species production, and therefore for methane output rate.

## 2.3 Electrochemical Laws

### 2.3.1 Faraday's Law

The law able to describe the electrochemical rates of production and consumption of species in a MEC takes the name of Faraday's Law [13]:

$$S_i = \pm \frac{M_i}{n_e F} R_{an/cat} \tag{2.7}$$

The species source or sink term $S_i$ is directly proportional to the species molar mass $M_i$ and the volumetric current $R_{an}$ or $R_{cat}$, for anode and cathode respectively. Therefore, it is clear the contribution of catalyzing methanogens able to increase the current densities on the electrodes, to achieve better rates. Furthermore, $S_i$ is inversely proportional to the number of exchanged electrons $n_e$ and the Faraday constant $F$.

### 2.3.2 Butler-Volmer and Tafel Equations

In fuel and electrolysis cells, the volumetric current terms may be identified by means of multiple equation, namely the Butler-Volmer (Eq. (2.8) and (2.9)) and the Tafel (Eq. (2.10) and (2.11)) equations, reported here following ANSYS FLUENT 12.0 Fuel Cell Modules Manual [14]. Basically, these electrochemical kinetics equations are able to describe a reaction rate by establishing a relation between the electrical current in the electrode and the overpotential.

$$R_{an} = (\zeta j_{an}^{ref}) \left( \frac{[A]}{[A_{ref}]} \right)^{\gamma_{an}} (e^{\alpha_{an} F \eta_{an}/RT} - e^{-\alpha_{cat} F \eta_{an}/RT}) \tag{2.8}$$

$$R_{cat} = (\zeta j_{cat}^{ref}) \left( \frac{[C]}{[C_{ref}]} \right)^{\gamma_{cat}} (-e^{\alpha_{an} F \eta_{cat}/RT} + e^{-\alpha_{cat} F \eta_{cat}/RT}) \tag{2.9}$$

$$R_{an} = (\zeta j_{an}^{ref}) \left( \frac{[A]}{[A_{ref}]} \right)^{\gamma_{an}} (e^{\alpha_{an} F \eta_{an}/RT}) \tag{2.10}$$

$$R_{cat} = (\zeta j_{cat}^{ref}) \left( \frac{[C]}{[C_{ref}]} \right)^{\gamma_{cat}} (e^{-\alpha_{cat} F \eta_{cat}/RT}) \tag{2.11}$$

- $\zeta$ Specific active surface area [$m^2$ $m^{-3}$]

- $j^{ref}$ Reference exchange current density per active surface area (A $m^{-2}$)

- [ ] and $[\ ]_{ref}$ local species concentration, reference value (kmol $m^{-3}$)

- $\gamma$ Concentration dependance

- $\alpha$ Transfer coefficient

- $\eta$ Overpotential [V]

Where "$[A]$ and $[C]$ represent the molar concentration of the species upon which the anode and cathode reaction rates depend, respectively" [14].

Lastly the overpotential $\eta$ for anode and cathode may be computed as:

$$\eta = \phi_s - \phi_l - E_{ref} \tag{2.12}$$

$$E_{ref} = 0\,\mathrm{V} \quad \text{Anode side;} \tag{2.13}$$

$$E_{ref} = E_{oc} \quad \text{Cathode side;} \tag{2.14}$$

$$E_{cell} = \phi_{s,cat} - \phi_{s,an} \tag{2.15}$$

## 2.4 Design and Operating conditions

In this Section, the areas of interest regarding the design and the operating conditions of a MEC will be presented. In addressing this topic, the work by Nelabhotla and Dinamarca [2] assumes a major role, as it shares many characteristics of its design with the desired features of the new reactor, whose model will be developed in Section 5

### 2.4.1 Influent

In the considered studies, the most common influent, which may be identified as the primary "fuel" for methane-producing MECs, is represented by wastewaters containing an organic load, i.e. organic molecules dissolved in a dilute water solution. A predominant component of such reject waters, which may come from a treatment plant or an AD, is acetic acid, $CH_3COOH$, also referred to as acetate, $CH_3COO$. Therefore, experimental setups either exploit samples of "reject water obtained from a local wastewater treatment plant" [2], coupled with phosphate buffer for pH control, or recreate artificial solutions with similar characteristics. An example of the latter is the work by Cheng et al., where the reactor was "operated with acetate (1 g/L) in a buffered nutrient medium (100 mM phosphate buffer solution (PBS)" [1]. Furthermore, also in the work of Rader and Logan, later adopted as Reference Study in Chapter 4, the MEC was fed with a substrate containing 1 g/L acetic acid, a 50 mM phosphate buffer solution.

#### COD

Many studies often refer to Chemical Oxygen Demand COD as an additional parameter to describe the influent solution characteristics. COD is crucial indicator in characterizing the quality of a liquid stream, such as reject water, since it allows to estimate how much organic matter, regarded as a pollutant, is present. In their work, Khan and Ali define COD as "the estimate of oxygen required for the portion of organic matter in wastewater that is subjected to oxidation" [15], therefore how much oxygen needs to be consumed if the organic matter present has to be degraded to carbon dioxide and water.

For acetic acid case, calculation may be carried out by balancing Equation (2.16) and solving (2.17), where $n_{O_2}$ represents the balanced moles of oxygen, while $M$

are the respective molar masses of acetic acid and oxygen [16].

$$CH_3COOH + 2O_2 = 2CO_2 + 2H_2O \tag{2.16}$$

$$\text{Equivalent COD} = \frac{n_{O_2} M_{O_2}}{M_{CH_3COOH}} = 1.07 \tag{2.17}$$

### 2.4.2 Yield

In this Section, the methane yield of two studies is presented. In both cases, the results accounts both for acetoclastic and hydrogenotropic methane. Nelabhotla and Dinamarca have been able to quantify the increase due to hydrogenotropic $CO_2$ reduction in 15%, while Rader and Logan did not focus on this distinction, since the original purpose of their paper was hydrogen production.

**Table 2.1:** Size and normalized yield of MEC from literature

| Paper | Size [$L_{WW}$ / day] | Methane Output [$L_{CH_4}$ / $L_{WW}$] |
|---|---|---|
| Nelabhotla and Dinamarca [2] | 0.135 | 0.54 |
| Rader and Logan [4] | 2.4 | 0.1 |

Furthermore, it may be pointed out that the work by Nelabhotla and Dinamarca was aimed at the optimization of two crucial working condition for electrochemical methane production: electrodes potential and pH. Respectively, the optimized values fall between $-0.7\,\text{V}$ and $-0.6\,\text{V}$, and around a pH of 7.0.

### 2.4.3 Design

#### Single chamber

The single chamber feature allows for a compact design, with the possibility to install multiple electrodes that may be placed sequentially or concentrically. Furthermore, the absence of a double chamber environment and the subsequent membrane implies the possibility of methane production following not only the hydrogenotropic pathway, but the acetoclastic one as well, as argumented by Cheng

et al. [1]. This may represent an advantage since the same reactor environment may be exploited by multiple phenomena concurring to methane production.

### 2.4.4 Membrane-less

The membrane-less feature is linked with the single chamber design, and allows for a cheaper reactor, since no ion-exchange membranes are needed.

#### Electrolyte

The role of the electrolyte may interestingly be covered by the wastewater itself, that enter from the reactor inflow carrying an organic load. Successively, the organic matter is broken down by oxidation to carbon dioxide, which is ready to be reduced at the cathode. The protons formed at the anode are then transported by the same wastewater flow to the cathode. Here protons and electrons, transported by solid current conductors are matched again to reduce $CO_2$ and finally form methane.

#### Continuous flow

Continuous flow may represent a crucial development to improve productivity of such technology. However, special attention must be paid to the hydraulic retention time (HRT), defines as:

$$\text{HRT [s]} = \frac{\text{Reactor Volume V [m}^3\text{]}}{\text{Volumeflowrate}\dot{\text{V}}\ \text{[m}^3\ \text{s}^{-1}\text{]}} \tag{2.18}$$

Low HRTs, below 5.3 hours [7], have not been yet tested and may induce the risk of washing out the microbial film that builds up on electrodes, catalyzing the whole process. Therefore, a balance between flow rate and HRT will to be experimentally assessed in the future, to gain more knowledge about the existence of a lower bound for HRT, and in order to maximize productivity.

### Electrodes material

An important step oriented toward scaling-up and marketability is represented by testing cheaper materials for electrodes. In the work by Sangeetha et al. [17] where wastewater from a beer plant are treated, a stainless steel cathode is compared to nickel and copper, producing convincing results.

Compared to the platinum-coated titanium mesh by Van Eerten-Jansen [10], the use of simple stainless steel meshes, replacing also graphite cloth and brushes, is key goal in order to lower the costs associated with this technology.

## 2.5 Efficiencies

The goal of this thesis does not consist in establishing the efficiency of process. However, a method to evaluate energetic efficiency is presented, along with experimental results from the available literature.

In their work, Van Eerten-Jansen [10] indicate Energy efficiency as the product of Coulombic and Voltage efficiencies, respectively $\eta_{CE}$ and $\eta_{voltage}$:

$$\eta_{energy} = \eta_{CE}\ \eta_{voltage} = \frac{-\Delta G_{CH_4} \cdot V_{CH4}}{V_m \cdot E_{cell} \cdot \int_{t=0}^{t} I dt} \tag{2.19}$$

$$\eta_{CE} = \frac{V_{CH4} \cdot n \cdot F}{V_m \cdot \int_{t=0}^{t} I dt} \tag{2.20}$$

$$\eta_{voltage} = \frac{-\Delta G_{CH_4}}{E_{cell} \cdot n \cdot F} \tag{2.21}$$

In the reported equations, Coulombic efficiency stands for the "efficiency of capturing the electrons from the electric current in methane" [10]. Furthermore, $V_{CH_4}$ is the cumulative methane gas production, $V_m$ is the molar volume, $I$ the current, $t$ the time. On the other hand, "Voltage efficiency, the amount of external electrical energy that ends up in methane, was calculated via the Gibb's free energy of oxidation of methane over the electrical energy input of the MEC $E_{cell}$" [10].

Focusing on experimental results, Cheng et al. reported an electron capture efficiency of 96% [1]. Furthermore, Nelabhotla and Dinamarca achieved a 98.9%

efficiency when supplying electrons for electrochemical CO2 reduction to methane [2].

The efficiency of energy recovery in the study by Rader and Logan [4] is based both on electrical and organic inputs, and has been presented in Chapter 4.

## 2.6 Applications

The last section of this overview on the electromethanogenesis is set to present various applications, already tested or only proposed.

The paper by Aryal et al. identifies biogas upgrading [18] as a possible application for BES, in order to produce biomethane by $CO_2$ reduction.

The work by Blasco-Gómez et al. proposes and reports multiple possible applications: on side the use for renewable energy storage, with concept of Bioelectrochemical Power-to-Methane; while at the same time waste treatment may benefit from the coupling Anaerobic Digestors (AD) with electrochemical methanation of the residual wastewaters [5] exiting the AD. The idea of exploiting microbial communities for waste treatment is present also in the work of Gil-Carrera et al., documenting the "Reduced energy consumption during low strength domestic wastewater treatment in a semi-pilot tubular microbial electrolysis cell" [19].

Cheng et al. already demonstrated the possibility that:

> Use of Archaea for producing methane via electromethanogensis provides an additional route for biofuel production accompanied with carbon dioxide capture, without the need for precious metal catalysts. The use of a methanogenic biocathode enables methane production from any electrical source, although renewable energy sources would provide the greatest advantages for truly sustainable energy systems. For example, the use of excess solar or wind energy or an microbial fuel cell could provide current for an MEC, producing methane that could be later reused to generate electricity or used as a transportation fuel. Existing industrial waste gases could provide CO2 sources for capture. Transforming electrons

into methane has the advantage of producing a fuel that can easily be stored or transported [1].

Nelabhotla and Dinamarca described the possible increase in methane production when integrating a MEC to AD, by installing a microbial reactor in the reject water loop. This approach could "improve the efficiency and productivity of existing waste/wastewater treatment plants" [2]. Furthermore, the biogas produced without applying an electrochemical potential to the reactor, yielded concentrantion of methane consistently lower than 90%, "whereas for MES operation it has been consistently above 90%" [2].

Lastly, the versatility of this technology is represented by the many fields in which it could be applied, ranging from treatment plant, as already seen, to beer wastewater. This has been applied in the work by Sangeetha et al., dealing with a microbial electrolysis-assisted AD reactor [17].

It seems noteworthy to point out that in the summer of 2022 when this thesis is being written, the cost of energy around Europe is experiencing strong increases. Solutions and applications as the ones briefly presented here may indicate a path toward the valuing of energy sources not yet fully exploited. As a matter of fact, the organic load in wastewater from treatments plant and industry applications still represent a burden, as it needs to be disposed correctly not to pollute the environment. Instead, the catalyzing actions performed by microbial communities in converting organic matter to methane may represent a robust procedure to accomplish power-to-gas transformations, in order to store more efficiently the not-constant energy supplied by renewable sources, while at the same time carrying out required treatment procedures. At the same time $CO_2$ sequestration may represent an additional accomplishment possible with this technology.

# Chapter 3

# Theory of Computational Fluid Dynamics

## 3.1 Numerical Simulation Workflow

In order to develop a robust numerical model for CFD, the steps to follow may be summarized according to the concepts presented in the "*Numerical Flow Simulation*" course (EPFL Master's Degree) held by Prof. Boujo [20]. The three main stages of the proposed workflow consist of:

1. Pre-processing: The major steps involved in this stage are the design of the geometry enclosing the fluid flow, i.e. the ducts and the reactor, and the meshing of the fluid regions;

2. Computation: The physical phenomena taking place in the fluid region are described by the selected governing equations, which successively undergo discretization in order to obtain a solution according to the Finite Volume Method.

3. Post-processing: Lastly, the numerical results are ready for visualization and quantitative analysis, to evaluate and comment the quality of the simulation. A fundamental analysis is represented by the convergence study, which

investigates how the results vary with respect to the number of mesh elements.

### 3.1.1 Pre-processing

#### Geometry

The first operation to be performed focuses on the geometric modeling of the region affecting the fluid flow. A wide variety of geometries may be involved, as the problem of interest may range from a closed conduit flow, taking place inside pipes, to the air flow around a car. The model developed in this thesis deals with a liquid flow entering a reactor chamber, in which methanation will take place, causing the presence of a secondary gas phase. Furthermore, porous electrodes will be present inside the chamber, and has to be included in the geometry.

From the CAD model of the reactor and the ducts connected to it, the fluid domain will be "*extracted*", in order to setup the simulation in the regions enclosed by the materials (i.e. walls, pipes). For the simulation to work, the geometry has to be "*watertight*", so that fully encloses the volume of fluid, and the flow enters and exits only from the intended inlets and outlets.

#### Mesh

Once the fluid domain has been obtained from the geometry of the model, it is possible to divide in into smaller control volumes, in which governing equations will be discretized and solved according to the methods presented later. The process of splitting the fluid domain into elements takes the name of Meshing, and may be executed following various methods, depending on the desired shape of the cells.

With the three-dimensional fluid domain involved in this simulation, the method of interest is the creation of hexahedral elements, with 8 nodes and 6 faces. Each type of element (tetrahedron, prism, polyhedron) affects differently the numerical approximation of gradient and fluxes. In this case, the use of a "*structured*" mesh composed by hexahedral cells may be more accurate, while reducing the the number of elements and subsequently the computational cost. Furthermore, "Numerical

diffusion is minimized when the flow is aligned with the mesh. This is the most relevant to the choice of the mesh. If you use a triangular/tetrahedral mesh, the flow can never be aligned with the mesh. If you use a quadrilateral/hexahedral mesh, this situation might occur, but not for complex flows. It is only in a simple flow, such as the flow through a long duct, in which you can rely on a quadrilateral/hexahedral mesh to minimize numerical diffusion. In such situations, it is advantageous to use a quadrilateral/hexahedral mesh, since you will be able to get a better solution with fewer cells than if you were using a triangular/tetrahedral mesh" [21].

The structured feature, introduced before, relies on sets of lines not crossing each other, while crossing different sets only once. This allows a simple neighbor connectivity coupled to an efficient solution of algorithms, even if difficulties arise with complex geometries and local refinements. The latter problem may be addressed by using block-structured meshes, split into sub-domains with a block-wise refinement.

A good mesh with an appropriate distribution should be able to provide the required level of detail, which may vary depending on the region. For example, electrodes regions usually feature very fine and thin materials: in this areas the mesh could benefit from smaller elements. Furthermore, the size of the mesh is always a trade-off between accuracy and computational cost [20].

Various parameters are dedicated to quantitatively measure the quality of the mesh, as Aspect ratio, Orthogonality, Skewness, with indicated appropriate ranges.

### 3.1.2 Computation

#### Problem Setup

The governing equations describing the flow have to be implemented in the model. By default, ANSYS FLUENT solves continuity and conservation of momentum equations for every model [21], while additional equations such as energy conservation and species transport may be included. Eventually, additional scalar variables such as electric potential may be defined and solved in the fluid domain.

**Multiphase Flows** When dealing with flows which comprehend multiple phases, e.g. one liquid and one gas phase, dedicated models are able simulate this conditions, by providing to the model the parameters of their interaction, such as surface tension and drag.

### Flow Solution

CFD relies on the use of the Finite Volume Methode (FVM), as stated in the ANSYS FLUENT 12.0 Theory Guide [21]:

> "ANSYS FLUENT will solve the governing integral equations for the conservation of mass and momentum, and (when appropriate) for energy and other scalars such as turbulence and chemical species. The control-volume-based technique used consists of:
>
> - Division of the domain into discrete control volumes using a computational grid. To each control volume a computational node is assigned.
> - Integration of the governing equations on the individual control volumes to construct algebraic equations for the discrete dependent variables such as velocities, pressure, temperature, and conserved scalars. *(The unknowns are discretized with nodal values).*
> - Linearization of the discretized equations by iterative methods and solution of the resultant linear equation system textit(matrix) to yield updated values of the dependent variables. textit(The terms of the governing equations are approximated as a function of the nodal values, both for volume and face integrals)."

**Boundary Condition** For the solution of non linear systems of equations as the ones involved in CFD, it becomes necessary to specify boundary conditions. Common sets on BC may feature the in-flowing mass flow rate and and the outlet pressure. Furthermore, walls are modelled as no-slip, and could also be set as

adiabatic to model an ideal heat flux equal to zero. Lastly, if symmetry planes are present, symmetry BC may be inserted. If chemical species are present, the mass fraction present at the inlet may be specified.

**Solution Initialization** To start the iterative procedure and obtain numerical results, the solution must be initialized by imposing initial values to the variables in a region of the fluid domain. For example, this may be done by setting the velocity, pressure, temperature and other variables at the inlet.

**Convergence monitoring** Once the iterative solving procedure has started, "*residuals*" are used to monitor the solution. "In a CFD analysis, the residual measures the local imbalance of a conserved variable in each control volume. Therefore, every cell in your model will have its own residual value for each of the equations being solved" [22]. The threshold used to judge residuals is usually set to $10^{-6}$, below this value the solution is considered to have converged.

An additional way to monitor convergence is by focusing on variable of interest, such as outlet pressure or a species mass fraction at the outlet, after reaction inside the reactor as in this thesis. Monitoring the variable, if it stabilized to a certain value as the iterations progress, convergence may be considered achieved.

### 3.1.3 Post-processing

#### Visualization

The numerical results may be presented by means of graphics, e.g. by visualizing the velocity field inside a reactor, or the mass fractions of species reacting in the electrodes regions. Furthermore, pathlines and vectors could be additional ways to present the data from the CFD analysis. This also allows to investigate readily the nature of results, by checking if the values in a specific area the ones expected or not.

### Quantitative Analysis

After having completed the solution of the developed CFD model, if convergence has been met, numerical results may be commented and applied to the context in which the model has used. For example, the final purpose of the model proposed in this thesis is the optimization of an electromethanogenesis reactor, which could be achieved by analyzing the flow inside the reactor chamber and through the electrodes. Therefore, CFD analysis may serve as a powerful tool to predict improvements and modifications, before the actual manufacturing and experimental testing.

However, before a model could be considered trustworthy, the major step of Validation is required. In the context of the study, before optimizing the design of a new reactor, the CFD model should applied to the design of an existing reactor, whose experimental results have been published. Subsequently, the numerical results should be compared against the experimental ones, verifying their agreement. Only at this point a CFD analysis conduced upon a new design could be meaningful, as the confidence in the predictive capacity of the model has been incresed [20].

Furthermore, also Verification may be performed by checking that the governing equations are solved by applying the proper numerical methods. Verification deals with mathematical-based errors, regarding for example poor discretization or a coarse mesh. The technique described in the next Section deals with Verification.

### Mesh Convergence Study

Alongside with Validation, another analysis named "Mesh Convergence Study" has to be conducted in order to verify the quality of numerical results. Mesh Convergence focuses on the relation between the number of mesh elements and the variation of numerical results. As the number of mesh cells for the same geometry is increased, the solution is expected to be increasingly more accurate. The role of the Mesh Convergence Study, as the name suggests, is to verify the convergence of the numerical results, when the number of cells is varied. This could be achieved by producing a series of meshes with an increasingly higher number of elements, and comparing the values of one or multiple variables, e.g. by checking the value

of the output pressure at the outlet, or even by selecting multiple points in which the values of the variable are collected, building a profile. If the mesh has been generated following the major guidelines, a convergence in the analyzed results is expected as the number of elements increases, even if it may not monotnic

# Chapter 4

# Reference Study

In order to confidently apply the model developed in this work, it is mandatory to validate it by means of comparison with experimental data. As stated by Slater [23]: "Validation examines if the conceptual models, computational models as implemented into the CFD code, and computational simulation agree with real world observations. The strategy is to identify and quantify error and uncertainty through comparison of simulation results with experimental data".

Therefore, a selection was carried out in order to identify a study featuring the same electrochemical working principles and a design similar to the one desired for the new reactor, which will be supported by the aforementioned model being developed in this thesis work.

In conclusion, the model will be adapted to properly simulate the reference study output, while its main "frame", being constituted by the Governing Equations and the numerical Solution Methods, will be valid for any reactor design being successively developed, as long as it lies in the region of validity of the model.

## 4.1 Description

In the work of Rader and Logan [4], the scalability of a biogas-producing MEC is examined by operating a 2.7 L reactor equipped with 8 electrodes pairs. The

performance of the MEC was monitored with multiple quatities, such as electrical current and gas production, along with the removed COD from the influent WW.

The experimental MEC features a single-chamber membrane-less design, i.e. positive and negative electrodes are located in the same chamber, immersed in the electrolyte and not separated by a membrane permeable to ions. Furthermore, the electrolyte role is carried out by the liquid WW solution itself, mainly composed by water, in which ions are transported and can also diffuse. These characteristics closely match the features upon which the design of the new reactor would be based, therefore making the model being developed in this thesis work more robust.

The flow behaviour through the reactor is expected to be dual with respect to liquid and gas phase: as WW enters the chamber, it passes through the electrodes where acetate is consumed, and hydrogen and methane gases are produced. At this point the gas phase rises to the top of the chamber in a vertical motion, accumulating in the empty headspace of around 0.3 L, while the WW liquid phase continues its horizontal flow out of the MEC.

The experimental biogas production from acetate originally targeted hydrogen gas. However, over a 18-days interval, the final biogas composition after day 15 mainly consisted of methane, while hydrogen production dropped after the third day.

Therefore, even if conditions have not been optimized toward methane production, factors such as the geometry of the reactor, the multi-electrode design, the continuous flow regime and, lastly, the use of acetate as substrate, constitute notable properties making this study a valuable reference in the development of a MEC model.

Lastly, this study has been chosen over the one by Nelabhotla and Dinamarca [2], mostly because of the internal organization of the reactor, as the location of the electrodes were clearly stated. Furthermore, the flows inside the reactor, regarding both the liquid and the gaseous phases, are supposed to be more linear and neat, while in the experimental setup of Nelabhotla and Dinamarca consists of 135 mL Durant bottle, with inlet and outlet both located at the top. This inevitably causes

a much more chaotic flow, complicated by the coexistence of two phases exiting from the same outlet.

## 4.2 Geometry

The internal dimensions of the reactor are reported in Table 4.1, while Figure 4.1 and 4.2 are from the work of Rader and Logan [4] and illustrate the layout of the reactor, with a top view and a picture of the setup, respectively. Furthermore, Figure 4.3 and 4.4 contain 3D models of the MEC geometry, and they have been realized by means of SolidWorks [24].

**Table 4.1:** Internal dimensions of the reactor's chamber

| Length [cm] | Height [cm] | Depth [cm] | Empty bed Volume [L] |
|---|---|---|---|
| 26.7 | 8.8 | 11.5 | 2.7 |

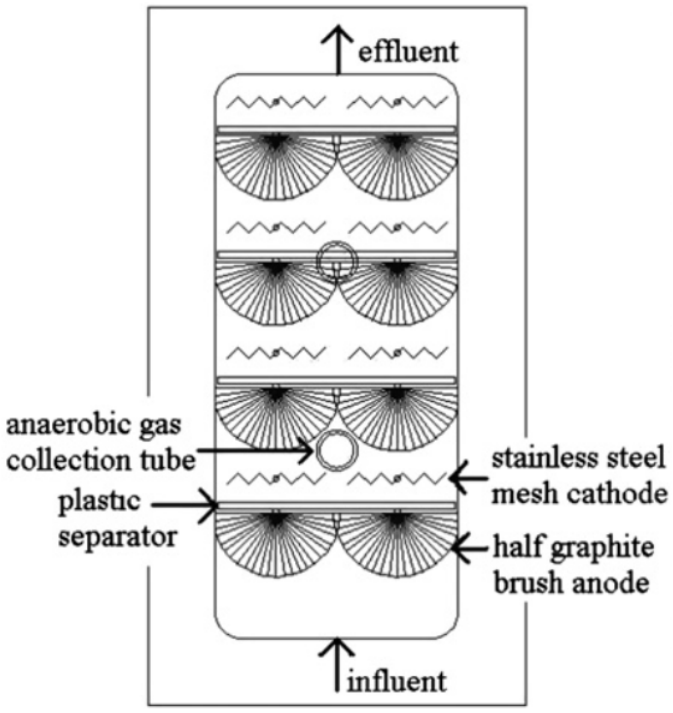


**Figure 4.1:** Top view of the MEC, from Rader and Logan study [4]

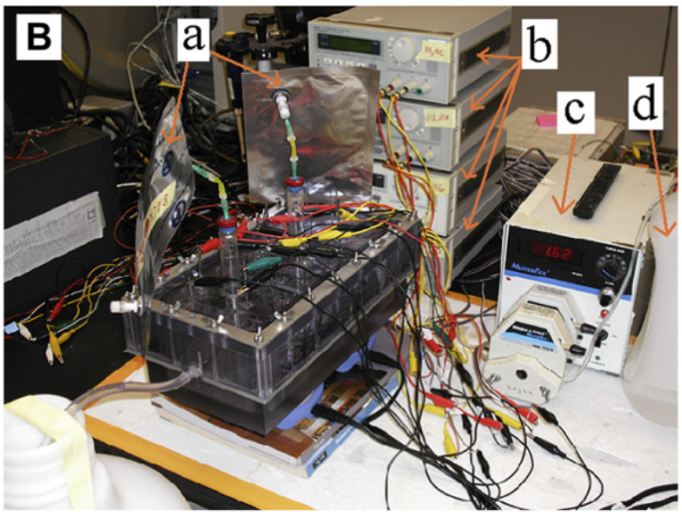


**Figure 4.2:** Picture of the MEC setup, from Rader and Logan study [4]

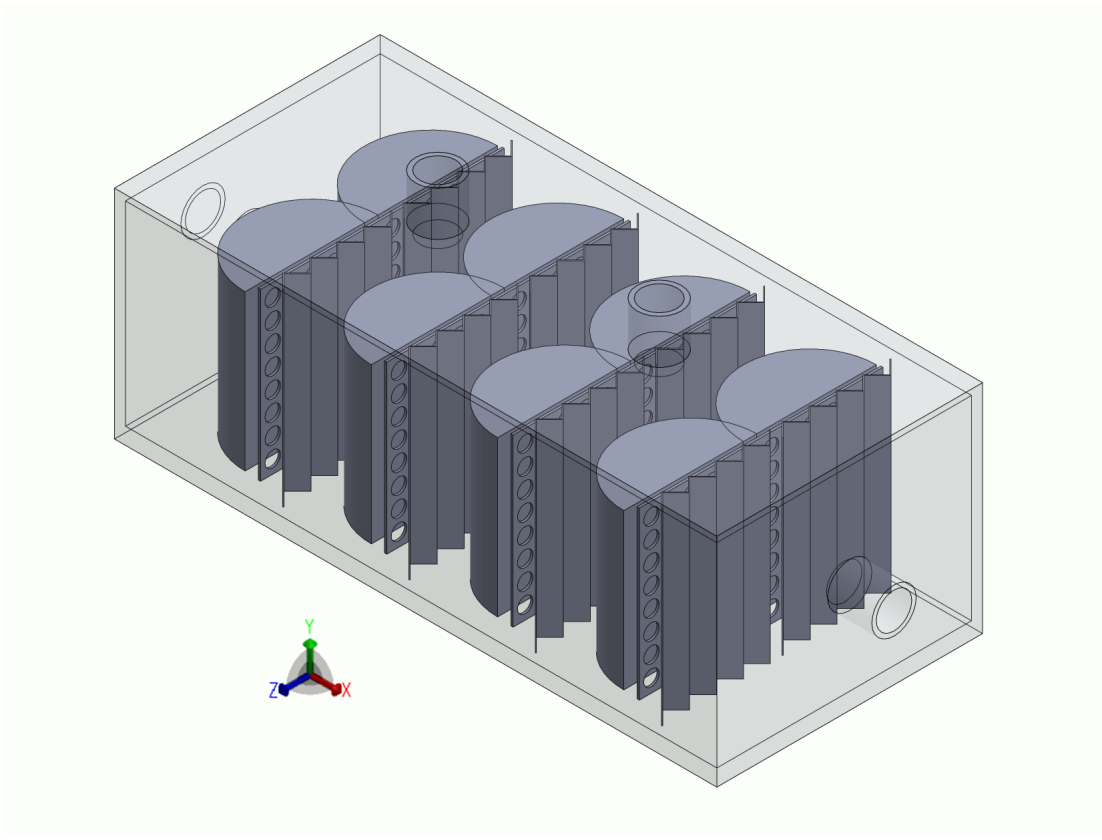


**Figure 4.3:** Isometric view of the MEC 3D model, recreated by means of SolidWorks

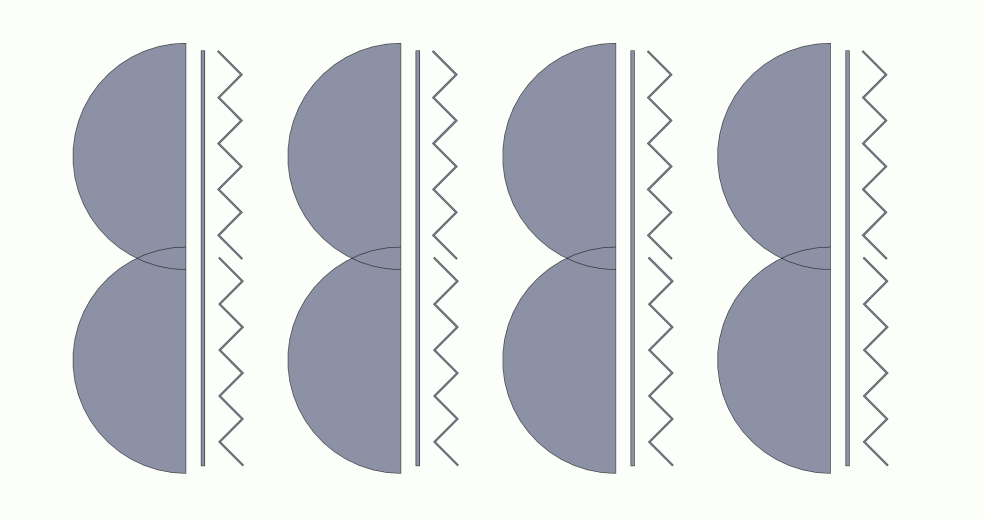

**Figure 4.4:** Top view of the MEC 3D model, recreated by means of SolidWorks

## 4.3 Electrodes

"Eight was selected as the number of electrode pairs because this was the highest number of electrode pairs, using the chosen electrode materials, that could fit in the reactor"

wire:
"The cathodes were connected to the circuit by a piece of 0.20 cm diameter titanium wire (McMaster-Carr) intertwined through two holes drilled through them, with the wire glued to the top of the reactor."

### 4.3.1 Anode

The material employed in the Reference Study for the anode is a graphite brush PANEX 35 50K, by ZOLTEK. The shape has been then altered by removing the fibers on one side [4], to finally obtain a semi-cylinder. The name "*50K*" indicates the filament count of the fibers, which are twisted around a titanium core [25].

The anode dimension has a diameter of 60 mm, and a height of 70 mm.

### 4.3.2 Cathode

The eight cathodes have been realized from a stainless steel 304 mesh sheet of size #60, from McMaster-Carr, Ohio. Sections of 8.5 x 9 $cm^2$ were realized and folded "along their width every 1 cm in an accordion-like fashion to increase total surface area" [4], as visible in Figure 4.1.

## 4.4 Operating Conditions

### 4.4.1 Wastewater composition

The main component of WW is clearly water, and its physical properties will be based upon the ones of liquid water. An initial anode inoculation was carried out in a MFC fed with acetic-acid to achieve anode acclimatation, with a medium composition of 1 g/L of acetic acid and a 50 mM phospate buffer solution. Later, "the MEC was operated with continuous substrate flow at a hydraulic retention time of one day" [4]. Therefore, the acetate present in the influent WW is quantified at 1 g/L.

Furthermore, the acetic acid equivalent COD is 1.07 g/L, as introduced in Section 2.4.1, which can be rounded to 1.1 g/L. This is consistent with the influent COD of 1.1 g/L indicated by Rader and Logan [4].

### 4.4.2 Wastewater Flow Rate

The MEC was operated in continuous-flow conditions, at a volume flow rate of 1.67 mL/min, equalling to 2.4 L/day, with a hydraulic retention time of 1 day. Therefore, the liquid volume present in the reactor was maintained around 2.4 L, leaving a headspace in the top part of the chamber for gas accumulation and collection through tubes.

### 4.4.3 Cell Potential

An electric potential of 0.9 V was applied by four separate power sources to each double pair of electrodes by means of two positive leads, connected to anodes, and two negative leads, connected to the cathodes.

## 4.5 Experimental Gas and Current Production

The experimental data relative to day 17 has been taken as the reference for model validation.

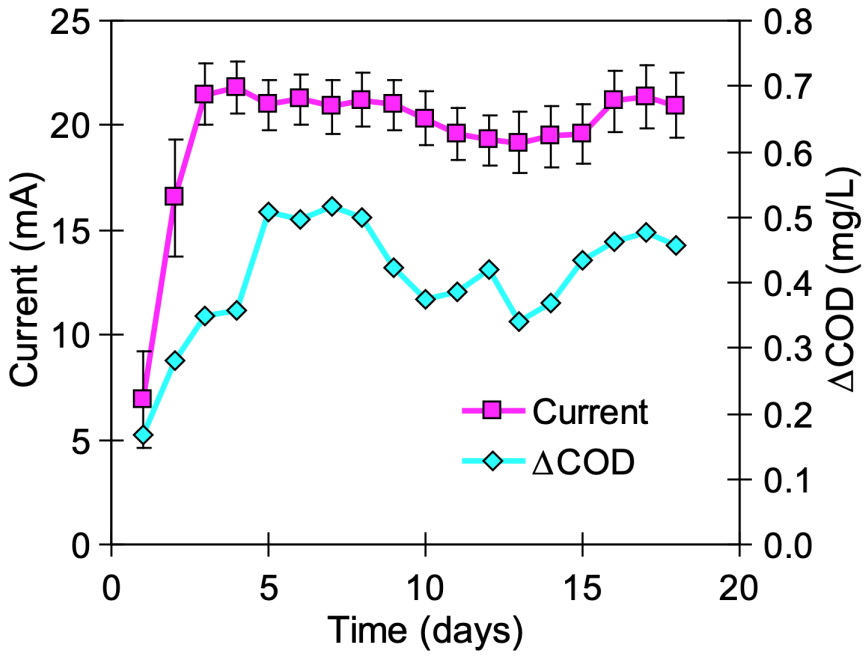


**Figure 4.5:** "Daily average current through the 8 electrode pairs and COD removal from the influent substrate (1.1 g/L COD)", from Rader and Logan study [4]

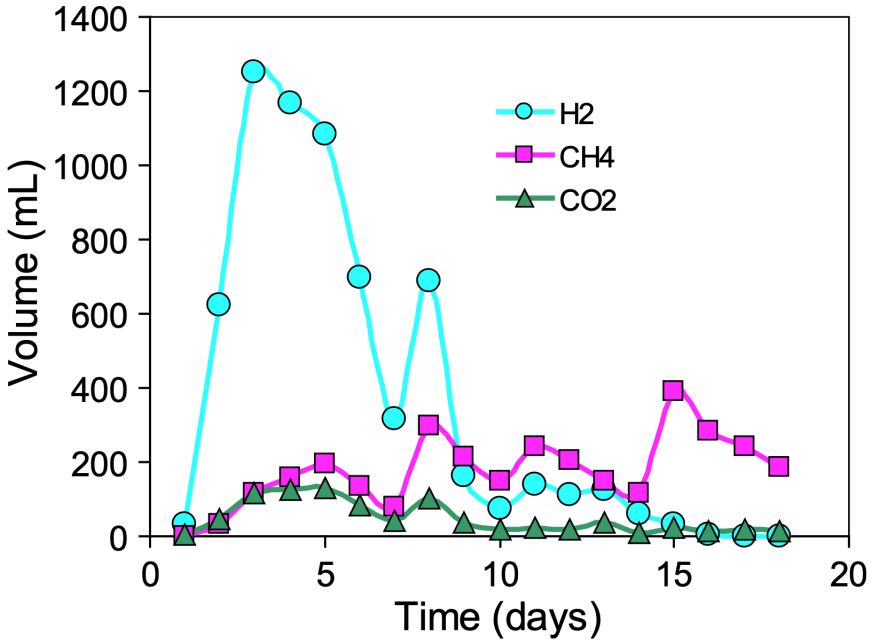


**Figure 4.6:** Hydrogen, methane, and carbon dioxide production over the 18 days of the experiment, from Rader and Logan study [4]

**Table 4.2:** Parameters of interest for CFD model validation

| Quantity | Value | Unit |
|---|---|---|
| COD removal | 0.48 | g $L^{-1}$ |
| Methane Output | 0.24 | L $day^{-1}$ |
| Current per electrodes pair | 0.22 | A |

## 4.6 Efficiency

Rader and Logan reported an energy efficiency of 30% on day 18, when taking into account both the electrical and the substrate energy inputs. The output energy was calculated by considering both hydrogen and methane being produced, with their Gibbs free energy. However, on day 18 only methane production was noted. Regarding the substrate, a substrate energy of −872.9 kJ/mol for acetic acid was assumed [4].

# Chapter 5

# Model Development

## 5.1 Model Objectives

In developing the model, the critical mechanisms that need to be simulated are mainly of two natures, which have been summarized in the two following objectives.

**Objective 1: Electrochemistry**

On one side, the electric potential applied at the electrodes' terminals (wires) of the MEC causes the presence of electrons and protons, modeled by two potential scalar fields, $\phi_s$ and $\phi_l$, which then define the overpotentials, and lastly the volumetric transfer currents. The volumetric transfer currents go on being proportional to the species source and sink rates, describing the species consumption and production. Therefore, the first goal of the simulation is being able to trace the production of methane back to the electrochemical parameters, i.e. applied potential and electrodes' specific surface areas.

**Objective 2: Multiple phases**

At the same time, the study taken as reference for model validation features a headspace located in the upper part of the reactor. This region will house the produced gases accumulating as they rise from the cathodes. Even if internal

motion of the fluids is clealry more complicated, a first simplification can be based on the different directions of flows: the liquid phase goes through the reactor mainly horiontally, while the gas phase forms at the electrodes as bubbles, rising to the top vertically due to gravity and lastly exiting the chamber from vertical upper gas outlets. Consequently, it is needed to model multiple phases, namely liquid WW and methane gas, to analyze the interactions between them.

## 5.2 Electrochemical Assumptions

The working principle of interest is based on the oxidation of acetate at the anode, resulting in the production of carbon dioxide. Carbon dioxide is then reduced at the cathode, producing methane.

However, it is critical to point out that not all the methane produced by the reactor can be ascribed to the hydrogenotropic pathway of interest. As a matter of fact, the work of Nelabhotla and Dinamarca [2] was able to quantify the bio-electrochemical increase in the production of methane around 10-15%, specifically 13.6% in their optimized conditions, while the rest of methane comes from the acetoclastic pathway, therefore a more canonical digestion process not exploiting bio-electrochemistry.

For this reason, **only 15%** of the observed methane output by Rader and Logan has been assumed to be produced electrochemically, and modeled accordingly. On the other hand, all the removed COD, corresponding to acetate, is assumed to be oxidized at the anodes, producing the measured current. At the same time, at the cathode not all electrons will be used directly for methane production, but only the 15%, while the remaining part is assumed to form back acetate. This acetate formed back will be finally converted into methane by the acetoclastic microbial population present on the cathodes.

The rest of the current-producing electrons travelling to the cathodes are assumed to react with $CO_2$ forming back acetate. This "formed-back" acetate is assumed to be responsible for producing acetoclastically the rest of the experimentally collected methane. The two-step reaction (carbon dioxide to acetate, acetate to methane acetoclastically) will be omitted from the model, just imposing the final acetoclastic methane production in the cathode regions.

### 5.2.1 Relationship Current - Species Source - Volume

The data from Rader and Logan's study [4] taken as a reference to validate Obective 1 model includes species consumption (COD removal), daily gas volume flow-rates

and electrical current values. The aim of this thesis is to obtain matching results by applying the same input parameters.

However, these data is not expressed as volumetric with respect to the volumes of the electrodes. Contrarily, governing equations necessary for Fluent modelling are based on volumetric terms, such as volumetric current $R_{an/cat}$ [A m$^{-3}$] and species source and sink terms $S_i$ [kg m$^{-3}$ s$^{-1}$], e.g. to specify how much mass of a species is consumed per cubic meter of electrode per period of time.

Therefore, to assess if the numerical values match the experimental setup, in the next Section the expected volumetric quantities have been computed starting from the available data from the study, using the volumes of the simplified electrodes.

### 5.2.2 Theoretical Calculations

Theoretical calculations have been performed to determine the parameters not directly provided by reference study, such as species source rates of consumption and production, along with volumetric currents, in order to better understand the phenomena inside the MEC. This has been done in order to later assess in a more comprehensive way the quality of obtained numerical results.

#### Anode

The starting point for anode calculations has been the reported COD removal, quantified in 0.48 g/L for day 17. By applying the equivalent COD of acetic acid of 1.07, the removed acetate amounts to 0.449 g/L. With this value of acetate to be consumed at the anodes, the volumetric acetate sink rate has been evaluated as:

$$\text{Acetate sink rate [kg m}^{-3}\text{ s}^{-1}] = \frac{(c_{Acetate,in} - c_{Acetate,out}) \cdot \dot{V}_{WW}}{V_{anode}} \tag{5.1}$$

Furthermore, the electrochemical reaction consuming the moles of acetate will form moles of carbon dioxide in a 1:1 ratio. This allow to evaluate the Carbon dioxide source rate.

Once the species rates have been evaluated, the Faraday's Law allows to compute

the volumetric current term [A $m^{-3}$]. Lastly, by multiplying the volumetric current by the volume of the anode, the produced current [A] is obtained.

**Table 5.1:** Anode Theoretical Calculations

| Quantity | Theoretical Value | Units |
|---|---|---|
| Sink-rate Acetate $S_{CH_3COO^-,anode}$ | -2.27 x $10^{-5}$ | kg $m^{-3}$ $s^{-1}$ |
| Source-rate Carbon Dioxide $S_{CO_2,anode}$ | 1.69 x $10^{-5}$ | kg $m^{-3}$ $s^{-1}$ |
| Volumetric Current $R_{an}$ | 297 | A $m^{-3}$ |
| Current $I_{an}$ | 0.020 | A |

### Cathode

For the theoretical calculations relative to the cathode, the starting point has been the daily methane output reported by the Reference Study, quantified in 0.24 L/day for day 17. As previously reported, in the model developed in this thesis 15% of the aforementioned output is assumed to be electrochemically produced by $CO_2$ reduction, while the rest comes from the acetoclastic pathway using the acetate formed back from $CO_2$ at the cathode. Either pathway exploits a portion of the electrons produced at the anode; however, the performed theoretical calculation show that not all the available electrons are consumed, but only around half.

Based on the observed methane output volume flow-rate, species source rates are obtained by multiplying by the methane density and dividing by the volume of the electrode.

$$\text{Methane source rate [kg m}^{-3}\text{ s}^{-1}] = \frac{\dot{V}_{CH_4} \cdot \rho_{CH_4}}{V_{cathode}} \tag{5.2}$$

Furthermore, as already stated, $CO_2$ is either consumed by producing methane, or forming acetate, later turning in methane as well by means of hydrogenotropic methanogens. In both these reactions, $CO_2$ ends up forming methane with a 1:1 mole ratio. Therefore the methane output mole flow rate may be applied to $CO_2$ as well, to assess its volumetric consumption rate [kg $m^{-3}$ $s^{-1}$].

**Table 5.2:** Cathode Theoretical Calculations

| Quantity | Theoretical Value | Units |
|---|---|---|
| Sink-rate Carbon Dioxide $S_{CO_2,cathode}$ | -1.79 x $10^{-5}$ | kg $m^{-3}$ $s^{-1}$ |
| Source Methane $CO_2$ Reduction $S_{CH_4,cathode}$ | 9.78 x $10^{-7}$ | kg $m^{-3}$ $s^{-1}$ |
| Source Methane Acetoclastic $S_{CH_4,cathode}$ | 5.54 x $10^{-6}$ | kg $m^{-3}$ $s^{-1}$ |
| Volumetric Current $R_{an}$ | 314 | A $m^{-3}$ |
| Current $I_{cat,CO_2\ reduction}$ | 0.002 | A |
| Current $I_{cat,acetoclastic}$ | 0.009 | A |
| Total current $I_{cat}$ | 0.011 | A |

The comparison of source and sink rates, and volumetric currents associated to them, shows a disequilibrium of the current generated at the anode, and the one exploited at the cathode. Practically, an apparent coulombic efficiency of 54% is achieved, as around only half of the produced electrons are actually exploited for the formation of methane, using both the pathways proposed: acetoclastic and hydrogenotropic.

### 5.2.3 Flow regime

The Reynolds number allows to better assess the regime of the flow under examination. It is influenced by the density of the fluid $\rho$, the fluid velocity $v$, the hydraulic diameter $D$ and, lastly, the dynamic viscosity $\mu$.

$$Re = \frac{\rho v D}{\mu} \tag{5.3}$$

Due to the multiple phases present in the reactor, two different Reynolds Number have been computed, at the WW inlet where only the liquid phase is present; and in one of the gas outlets located on the top of the reactor, where on the other hand, only the gas phase is present.

**Table 5.3:** Reynolds Number

| Fluid | $\rho$ [kg/m$^3$] | $v$ [m/s] | $D$ [m] | $\mu$ [$10^{-6}$ Pa s] | Re |
|---|---|---|---|---|---|
| Liquid | 998 | 1.39 x $10^{-4}$ | 0.016 | 1003 | 2.21 |
| Gas | 0.657 | 1.38 x $10^{-5}$ | 0.016 | 11.2 | 6.48 |

From the evaluated Reynolds numbers, it may be argued with confidence that the flow regime inside the reactor is laminar, for both the phases that are present.

### 5.2.4 Species Solubility

In order to assess whether a gas phase will be present and what species will compose it, species' solubilities has been have been compared to their amount inside the reactor. Methane, by assuming a production of 0.24 L/day, as for day 17, correspond to a value three times greater than the solubility of methane in water a t 20°C, while carbon dioxide is well under the solubility threshold and will be completely dissolved in WW.

**Table 5.4:** Species solubility

| Species | Concentration [g/kg water] | Solubility at 20°C [g/kg water] |
|---|---|---|
| Carbon Dioxide | 0.36 | 1.5 |
| Methane | 0.066 | 0.023 |

Therefore, the gas phase in the model will be composed only of methane: as soon as carbon dioxide is reduced at the cathode, forming methane, the latter will exit the liquid solution and rise to the top in form of bubbles, accumulating in the chamber's headspace. As a consequence, the gas volume fraction in this upper region of the MEC will be equal to 1, meaning that only gas phase is present. This aspect needs to be carefully considered in the selection of a multiphase model, which must be able to model the vertical rise of bubble to the top, and the formation of a large horizontal-plane interface between gas and liquid phases.

## 5.3 Geometry

The reactor's geometry is based on the reference study selected, as presented in Chapter 4 and it has been modelled by means of the solid modeling CAD application SolidWorks [24]. The main features of reactor's design include external walls, inflow and outflow ducts, and the internal couples of electrodes.

The internal dimensions of the rectangular chamber have been taken equal to the ones provided by Rader and Logan [4] and reported in Table 4.1.

Furthermore, the inflow and outflow ducts have all been sized to a diameter of 16 mm, according to the previously stated characteristics.

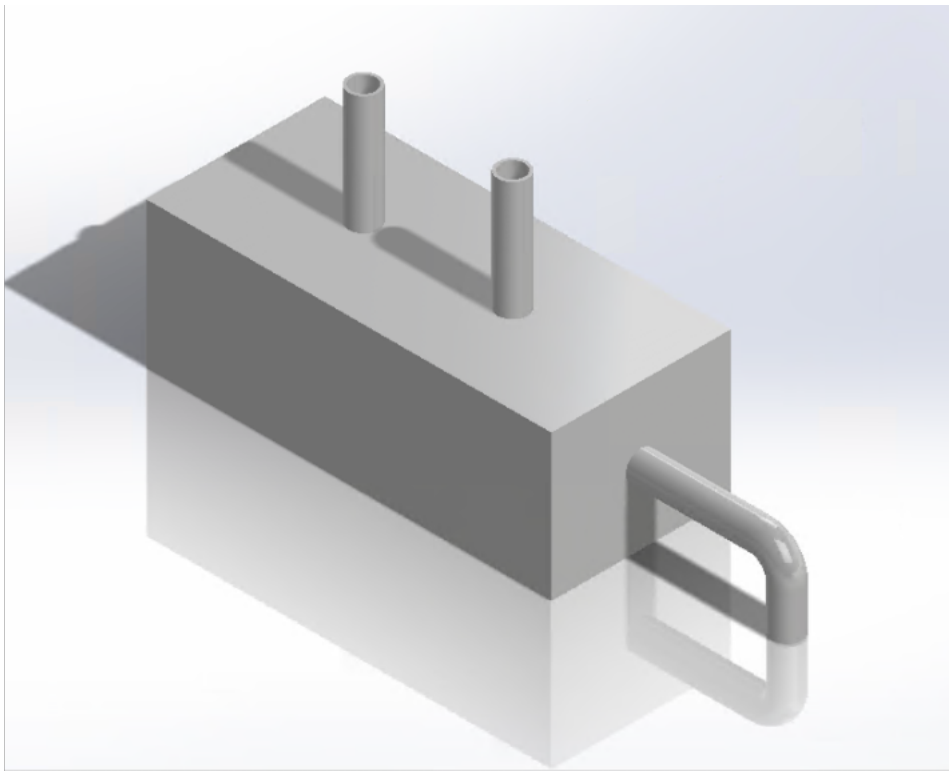

**Figure 5.1:** Isometric view of 3D model of MEC from Reference Study [4], adapted for CFD simulation; developed in SolidWorks

.

### 5.3.1 Simplifying Assumptions

Having considered the complexity of the original reactor, a series of simplifying assumptions have been introduced. This operation is intended to reduce the small-scale elements present in the final geometry, in order to later obtain a more homogeneous mesh with less local refinements.
A list of the modified elements is presented:

- Anodes, originally overlapping along the XY symmetry plane, were reduced in diameter from 60 mm to 50 mm.
- The original cathode's shape, featuring a stainless steel folded mesh sheet described as an "accordion-like fashion" [4], has been simplified to a cuboid, or rectangular prism. The selected dimensions are: 50 mm x 70 mm x 10 mm. Therefore, it is possible to highlight that anode and cathode feature the same width (50 mm) and height (70 mm) ; additionally, they will be aligned.
- Electrodes are positioned halfway between the bottom and the top of the reactor, therefore having the same distance from both of the walls.
- The multi-hole separator between each anode and cathode pair has not been included in the geometry, leaving a empty space between the two, completely filled by the working fluid.
- Electrodes' wire terminals have been modelled by removing a portion of each electrode's volume and placing a small cylinder on the top part of the aforementioned electrode, in a slot realized specifically for this purpose. The dimensions of the cylinder are a 2 mm diameter, in accordance with real circuit connectors, coupled to a 1 mm height. The wire terminal's slot had the same depth, therefore fully housing the solid cylinder.
- Outflow ducts feature a longer design compared to the inflow one, in order to try to reduce and eliminate the presence of unwanted "Reversed flows" in the numerical solution.

### 5.3.2 Final Geometry

The main characteristics that have been assumed to produce a final geometry for the reactor, which are either in contrast with the original reference or where not clearly stated, have been summarized in the following tables.

**Table 5.5:** Dimensions of the simplified design of electrodes

| Electrode | Shape | Size |
|---|---|---|
| Anode | Half Cylinder | ⌀50 mm x 70 mm |
| Cathode | Cuboid | 50 mm x 70 mm x 10 mm |

**Table 5.6:** Dimensions of the inlet and outlet ducts

| Duct | Lenght [mm] |
|---|---|
| Inlet | Horizontal 20 |
| Liquid Outlet | Horizontal 80 - Radius 30 - Vertical 30 |
| Gas Outlets | Vertical 80 |

The distance between the axes of the gas outlets is of 100 mm. Furthemore, the distance between the centers of anodes (or cathodes) of the same row, following the order from inlet to liquid outlet, is 60 mm.

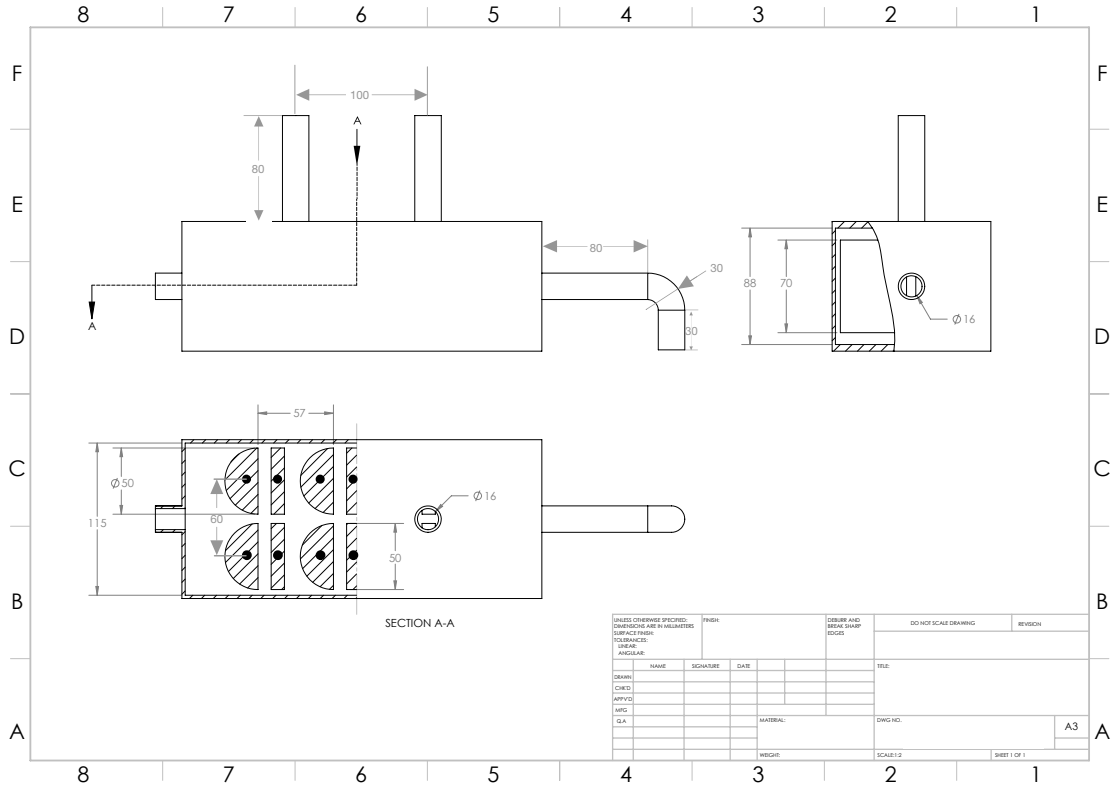


**Figure 5.2:** 2D Technical Drawing of the MEC from Reference Study, including dimension. The enlarged version is available in the Appendix A.1.

## 5.4 Meshing

The mesh for this model has been realized from the geometry presented at Section 5.3 by means of Ansys Meshing, available in the Workbench environment [26].

The global setting influencing the mesh resolution is the Element Size [m], which has been varied in Section 5.4.1 to obtain coarser and finer meshes among which a selection was carried out to choose the final mesh for the model.

The mesh has been designed as structured, by means of Ansys Meshing's MultiZone tool, able to provide "automatic decomposition of geometry into mapped (structured/sweepable) regions and free (unstructured) regions" [27]. In the structured regions a pure hexahedral mesh was generated, while the use of a free mesh type was not needed in any region. In order to obtain a fully structured mesh, the geometry had been split in multiple regions. This led to misalignment due to non-matching cell interfaces, that have been partially mitigated by the use of "Contact Sizing" and "Match Control" tools.

Lastly, the choice to include a small solid cylinder in top portion of every electrode, to simulate the presence of electrical wires, implied the presence of a small scale element. This has led to the perturbation of the homogeneous structured mesh, implying the need of smaller cells around the cylindrical elements, by affecting the cells positioned along the same vertical axis.

### 5.4.1 Grid Convergence Study

To assess the dependence of the numerical solution on the mesh resolution, four meshes were compared, with an increasingly higher number of elements, listed from 1 to 4. In order to analyze the results, the numerically computed values of acetate mass fraction were considered, to evaluate the Grid Convergence Index (GCI) of each different mesh. Following the work of El Ibrahimi et al. [28], a total of 1000 points were selected along a line passing through the electrodes, aligned with the x axis and positioned sideways from the wastewater inlet - liquid outlet direction. The selected points are located halfway between the top and the bottom sides of

the reactor, and halfway between the central x-y plane and the longer-side wall. The location of the line containing the selected points is shown in Figure 5.3 and 5.4, represented by velocity vectors hinged in the points' positions.

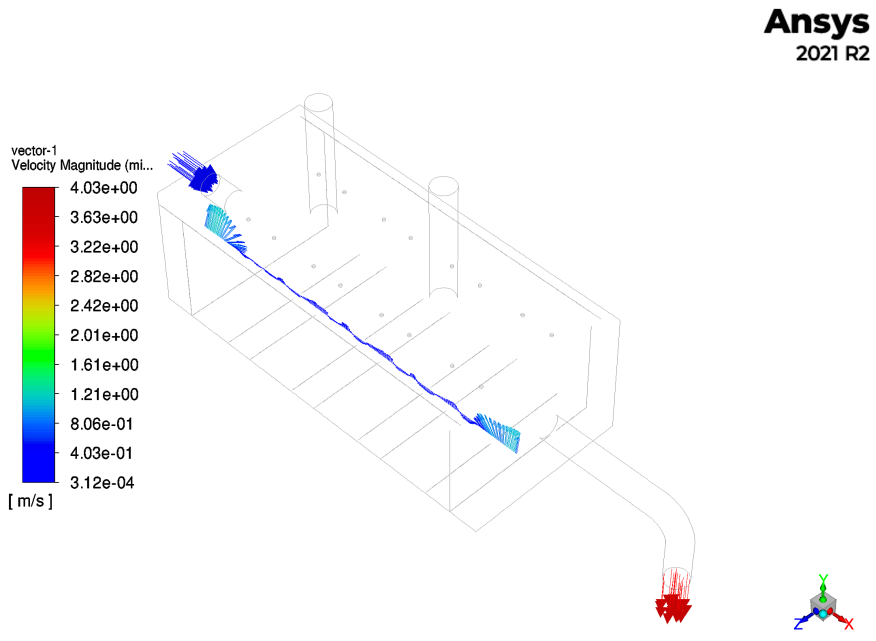


**Figure 5.3:** Isometric view of MEC, with line reporting the 1000 points considered for Grid Convergence Study.

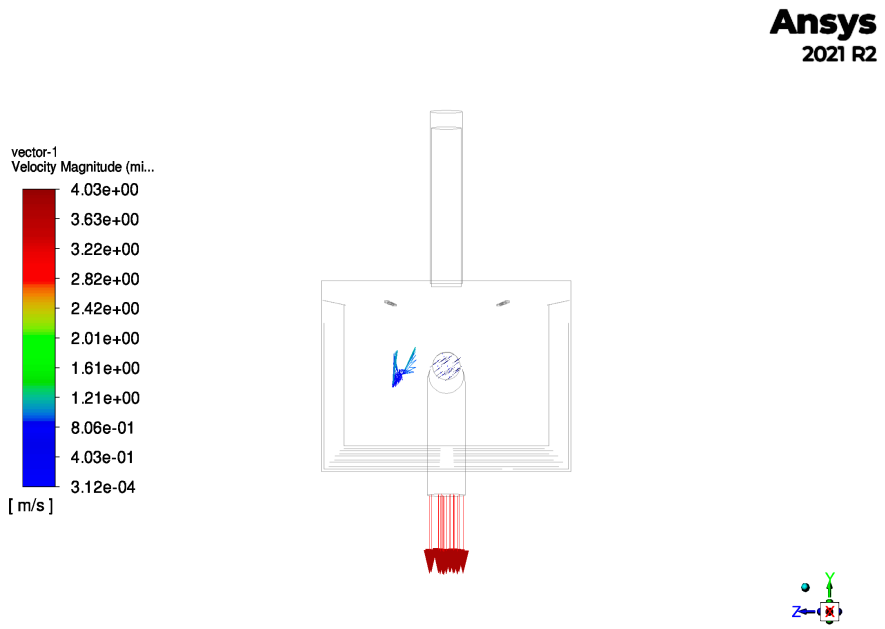


**Figure 5.4:** Front view of MEC, with line reporting the 1000 points considered for Grid Convergence Study.

**Table 5.7:** Meshes generated for the Grid Convergence Study; mesh number, mesh characteristic and number of elements

| **Grid Number** | 1 | 2 | 3 | 4 |
|---|---|---|---|---|
| **Mesh** | Baseline | Refined | | |
| **Elements Number** | 122,319 | 252,249 | 488,446 | 1,086,150 |

$$GCI_{1-j} = F_s \frac{RMSD_{1-j}}{r_{1-j}^2 - 1} \tag{5.4}$$

$$RMSD_{1-j} = \sqrt{\frac{\sum_{n=1}^{1000} |(Y_{n,1} - Y_{n,j})/Y_{n,j}|^2}{1000}} \qquad for \qquad 2 \leq j \leq 4 \tag{5.5}$$

$$r_{1-j} = \left(\frac{h_j}{h_1}\right)^{1/p} \tag{5.6}$$

In the presented equations, $F_s$ is a safety factor set to 1.25, $RMSD_{1-j}$ is the root mean square deviation between the baseline and refined meshes, r is the grid

refinement ratio, $Y_i$ is the acetate mass fraction in point $n$, $h$ is the number of elements, and $p$ is the dimensionality of the problem (equal to 3 for 3D models). Lastly, the subscripts 1 and $j$ are used to respectively identify the baseline and refined meshes [28].

**Table 5.8:** Grid convergence index values.

| Grid Convergence Index | $GCI_{1-2}$ | $GCI_{1-3}$ | $GCI_{1-4}$ |
|---|---|---|---|
| Values | 0.5790 | 0.4762 | 0.2837 |

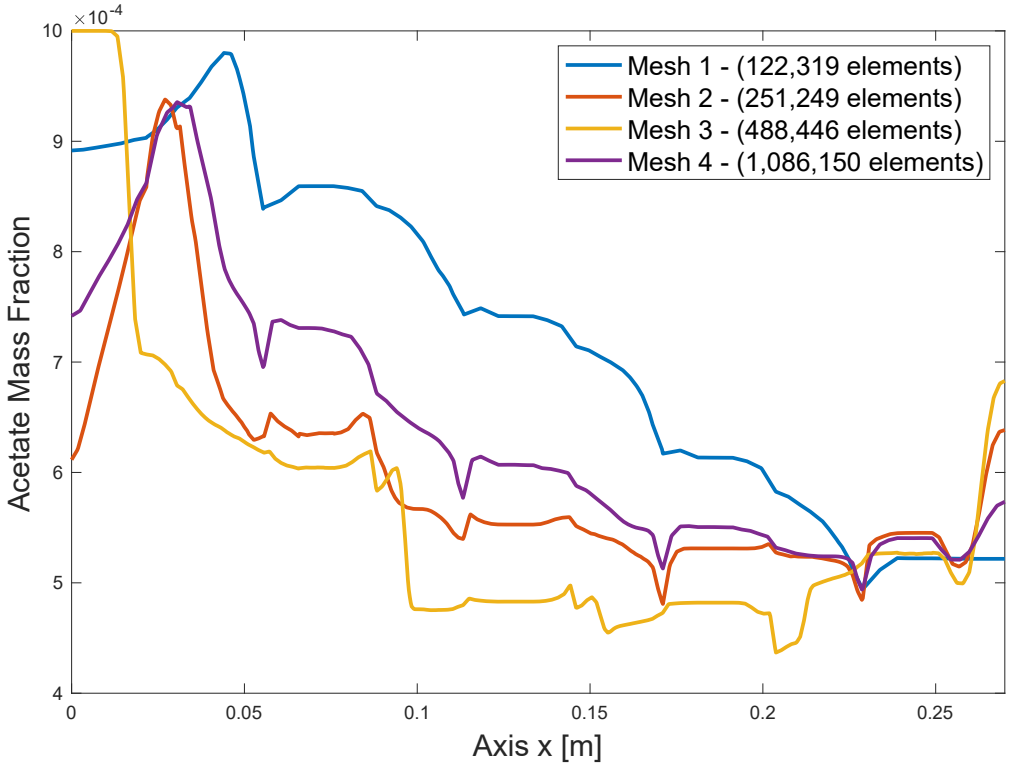


**Figure 5.5:** Acetate mass fraction of the 1000 points considered for Grid Convergence Study; the 4 meshes produced are reported in different colors.

Having set the coarsest mesh of 122,319 elements as the baseline, the GCI of the refined meshes has been evaluated, according to El Ibrahimi et al. [28]. Mesh 2

and Mesh 3 yielded a GCI of 0.58% and 0.48%, respectively. However, the small improvement in GCI of Mesh 3 does not justifies the higher computational cost implied by the presence of roughly twice the mesh elements. Lastly, even if Mesh 4 would grant a optimal GCI, the computational cost represented by more than 1 million elements is not sustainable.

### 5.4.2 Selected Mesh

The selected mesh is Mesh 2, featuring 251,249 elements. As stated in Section 5.4, the mesh is a completely structured, being composed of hexahedral elements. Furthermore, elements far from ducts and electrodes are fully cubes, featuring the highest orthogonal quality. The geometry around electrodes and solid elements (Figure 5.9) is more distorted, but as the histogram in Figure **??** shows, a good level of quality is still accomplished.

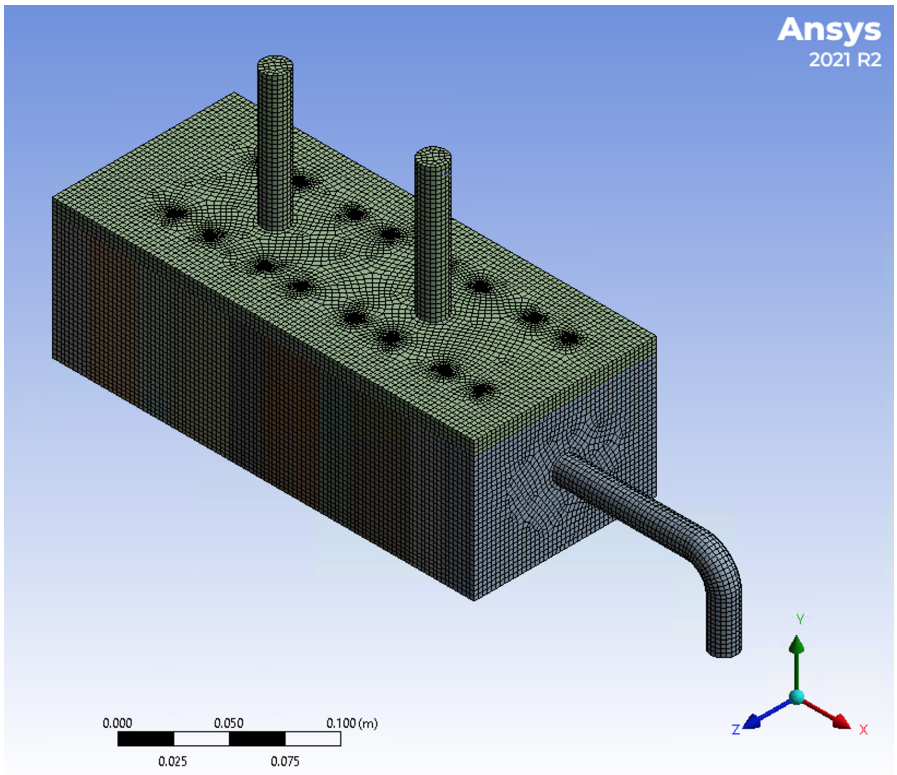


**Figure 5.6:** Isometric view of the MEC structured mesh.

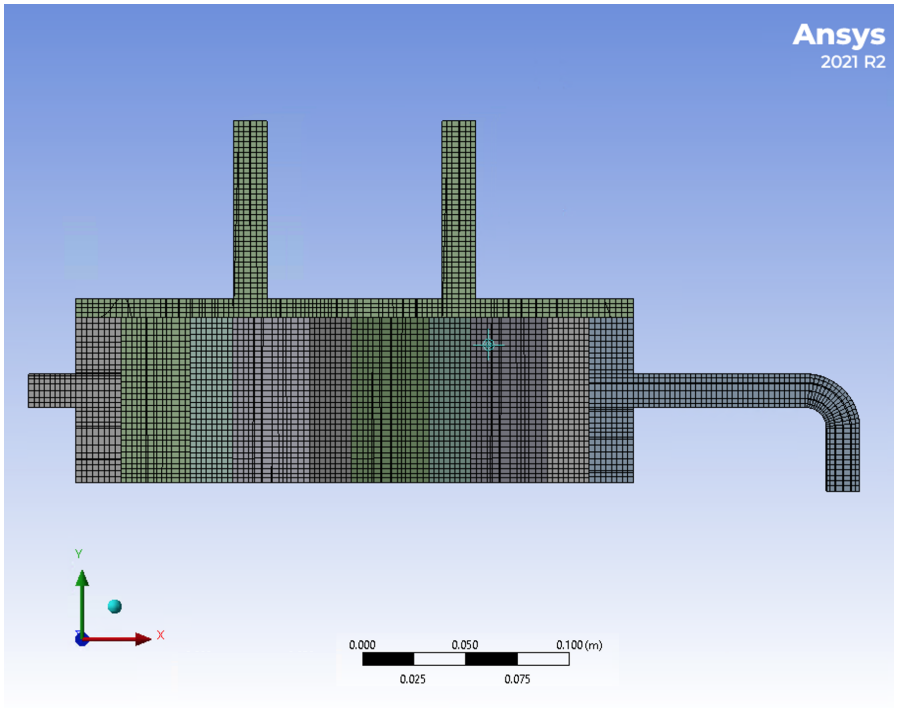


**Figure 5.7:** Side view of the MEC structured mesh.

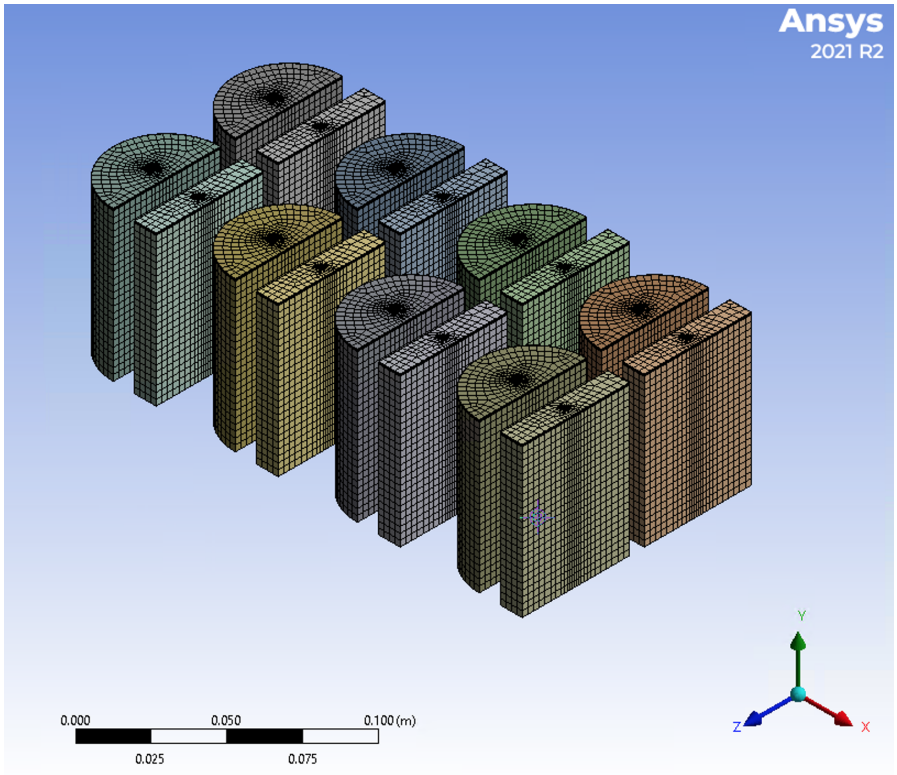


**Figure 5.8:** Isometric view of the MEC structured mesh, displying only the regions of electrodes, that will be modelled as porous media.

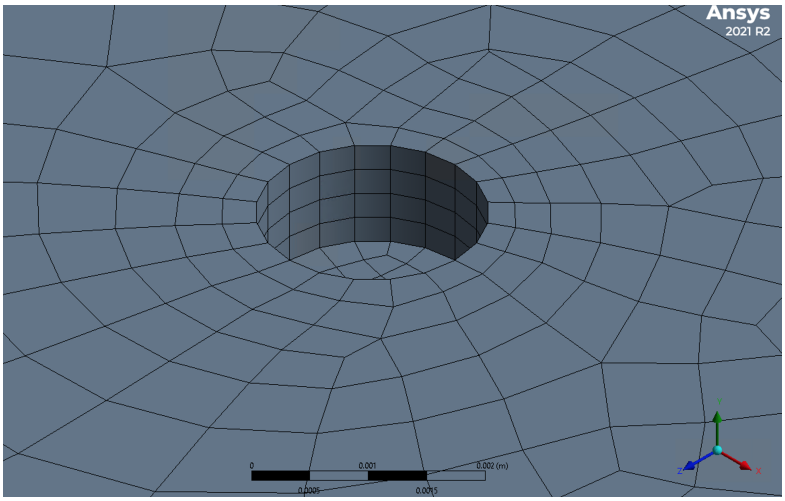


**Figure 5.9:** Isometric view on a detail: cylindrical empty space on the top of each electrode, modelling the presence of metal wire for current conduction. The presence of this detail perturbed the structured mesh around it, giving the visible elements deformation.

Figure **??** reports the quality of the selected mesh, grouping the elements in ranges of orthogonal quality. It is evident that orthogonal quality sits comfortably above 0.1, with a minimum of 0.65.

Furthermore, the shape of the cells is described by the Aspect Ratio: every zone of the mesh is below $35:1$ as prescribed [21], respectively 21, 20 and 10 in anodes, cathodes and fluid region.

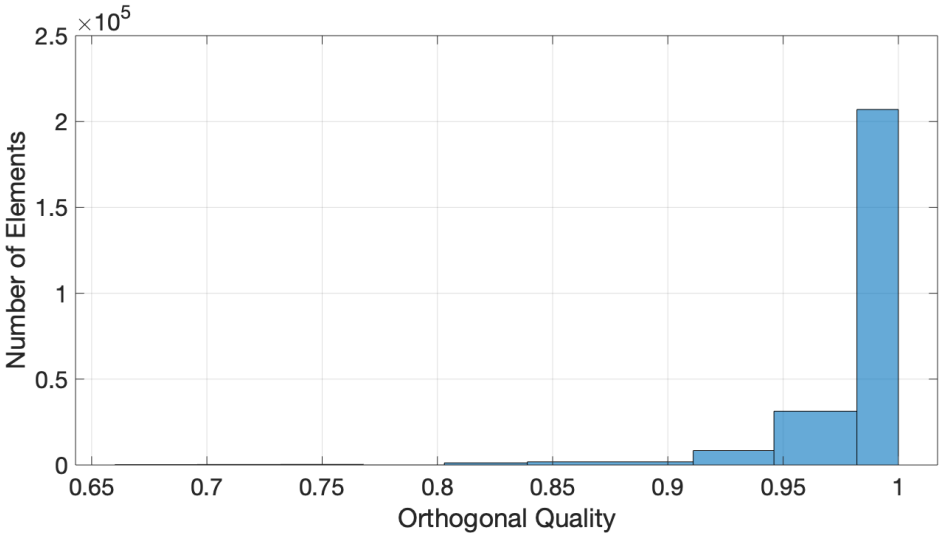


**Figure 5.10:** Orthogonal Quality of the mesh elements, sorted in groups according to their range of quality, with the quantity of each group on the y axis.

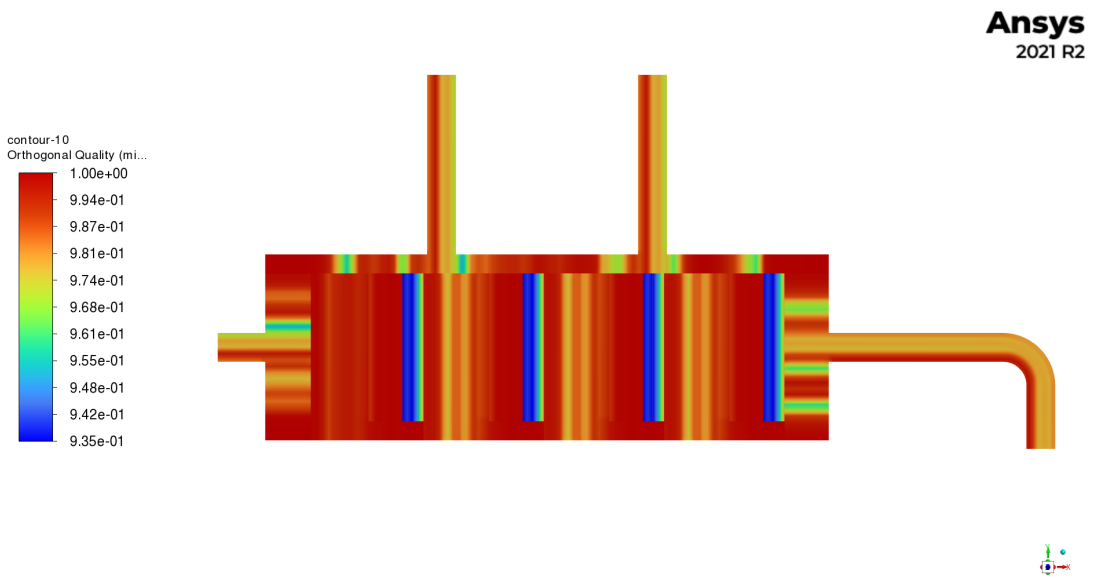


**Figure 5.11:** Orthogonal Quality of the mesh elements, on x-y symmetry plane. All the elements in this plane share an orthogonal quality above 0.93

### 5.4.3 Possible Mesh Improvements

Possible improvements to the generated mesh are proposed in this Section.

**Symmetry** On one side, the introduction of a symmetry boundary condition along the x-y plane could halve the number of mesh elements, effectively reducing the computational cost. This action should have no drawbacks, and its introduction is advised in the next version of this model, with any kind of reactor shape allowing to find a proper symmetry plane.

**Boundary layer** The second proposed modification to the mesh is based on the introduction of a boundary layer along the walls of the reactor. This is aimed to obtain more accurate modelling of the effects induced on the fluid flow by the reduced distance from the walls. However, the refined region close to the wall presents a trade-off with respect to computational cost, since the number of elements would be greatly increased.

In the following images, a mesh featuring a boundary layer of 5 inflation layers is presented.

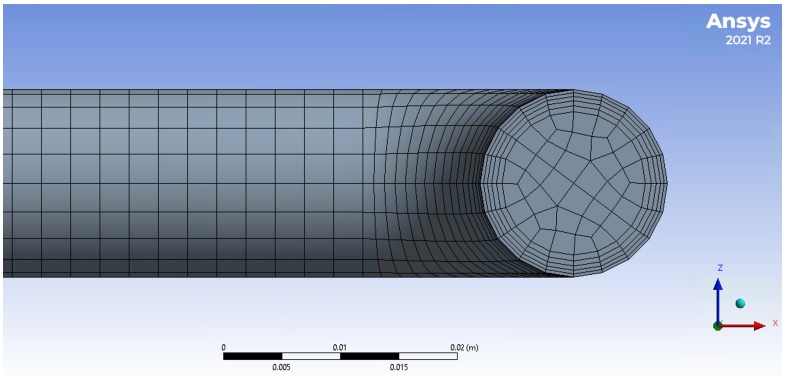


**Figure 5.12:** Boundary layer at the outlet duct

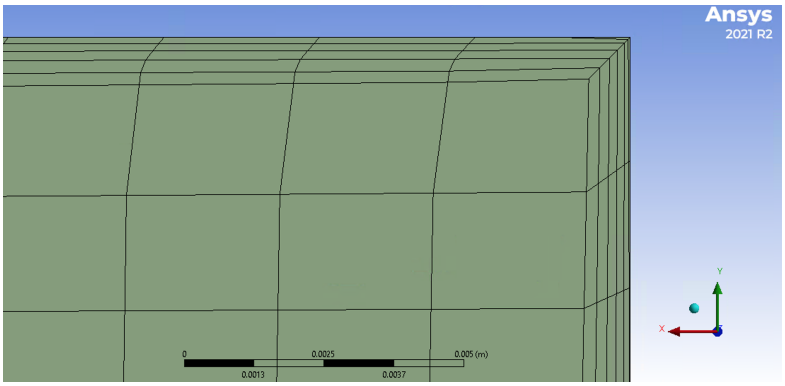


**Figure 5.13:** Boundary layer on a reactor edge

## 5.5 Mathematical Model

The study by Le and Zhou [29] served as the main reference in developing a mathematical model able to describe the waste-water's flow inside the MEC. This has been possible only by passing through a certain degree of adaptation, considering their model had been developed for the study of a proton exchange membrane fuel cell (PEMFC).

### 5.5.1 Model Assumptions

The main assumptions made in the development of the MEC model, once again following the work of Le and Zhou [29], are summarized here:

1. The simulation has been assumed as steady state, therefore time-dependent terms are not present in the governing equations.

2. Ideal gas law was employed for gaseous phase, constituted by methane gas. On the other hand, the liquid phase corresponding to wastewater has been modeled with constant density being equal to the one liquid water, due to the very dilute concentrations of substrate.

3. The fluid flow in the reactor has been assumed to be laminar due to the low flow velocities, as supported by the Reynolds Number below 10 both in the inflow duct and in the two gas vertical outlets.

4. Electrodes have been modelled as porous media. Therefore, anodes and cathodes' regions are not solely occupied by the flowing fluid, whose volume fraction is therefore lower than 1, as indicated by the porosity $\varepsilon$. Furthermore, these regions will include an additional source term for the momentum conservation equation, representing the pressure drop experienced by the fluid in order to overcome viscous losses.

### 5.5.2 Physical Properties

The physical properties and constants involved in the model have been summarized in Table 5.9.

**Table 5.9:** Physical properties and constants

| toprule Physical property | Value | Units | |
|---|---|---|---|
| WW Mass flow rate $\dot{m}_{WW}$ | 2.78 x $10^{-5}$ | kg $s^{-1}$ | |
| Acetate Concentration $C_{CH_3COO^-}$ | 0.001 | kg $L_{WW}^{-1}$ | |
| WW Density $\rho_{WW}$ | 998 | kg $m^{-3}$ | [30] |
| Methane Density $\rho_{CH_4}$ | 0.657 | kg $m^{-3}$ | [31] |
| Gravity Acceleration $g$ | 9.81 | m $s^{-2}$ | |
| WW Inlet Temperature $T_{in}$ | 293 | K | |
| WW Dynamic Viscosity $\mu_{WW}$ | 1.0016 | mPa s | [32] |
| Methane Dynamic Viscosity $\mu_{CH_4}$ | 0.0109 | mPa s | [33] |
| WW Specific Heat Capacity $c_{p,WW}$ | 998 | J $kg^{-1}$ $K^{-1}$ | |
| Methane Specific Heat Capacity $c_{p,CH_4}$ | 0.657 | J $kg^{-1}$ $K^{-1}$ | |
| WW Thermal Conductivity $k_{WW}$ | 0.598 | W $m^{-1}K^{-1}$ | [34] |
| Methane Thermal Conductivity $k_{CH_4}$ | 0.034 | W $m^{-1}K^{-1}$ | [35] |
| Anode Porosity $\varepsilon_{an}$ | 0.95 | - | |
| Cathode Porosity $\varepsilon_{cat}$ | 0.60 | - | |
| Open-circuit Voltage $E_{oc}$ | 0.9 | V | |
| Faraday constant F | 96,487,000 | C $kmol^{-1}$ | |
| Gas constant R | 8314 | J $kmol^{-1}$ $K^{-1}$ | |
| Acetate Molar mass $M_{CH_3COO^-}$ | 59.04 | kg $kmol^{-1}$ | |
| Carbon Dioxide Molar mass $M_{CO_2}$ | 44.01 | kg $kmol^{-1}$ | |
| Methane Molar mass $M_{CH_4}$ | 16.04 | kg $kmol^{-1}$ | |
| Anode Transfer Coefficient $\alpha_{an}$ | 0.5 | - | [36] |
| Cathode Transfer Coefficient $\alpha_{cat}$ | 0.5 | - | [36] |
| Anode Specific Active Surface $\zeta_{an}$ | 5300 | $m^2$ $m_{WW}^{-3}$ | |
| Cathode Specific Active Surface $\zeta_{cat}$ | 64 | $m^2$ $m_{WW}^{-3}$ | |
| Anode surface reference exchange current A concentration/ A reference concentration $j_{an}^{ref}\left(\frac{[A]}{[A_{ref}]}\right)^{\gamma_{an}}$ | 9500 | A $m^{-2}$ | |
| Anode surface reference exchange current A concentration/ A reference concentration $j_{cat}^{ref}\left(\frac{[C]}{[C_{ref}]}\right)^{\gamma_{cat}}$ | 40 | A $m^{-2}$ | |
| Surface Tension $\chi$ | 0.075 | N $m^{-1}$ | |

### Electrodes Porosity

Electrodes are modeled as porous media, representing a region not fully occupied by the fluid phase, but instead where solid materials and fluid coexist. Porous media modeling will have further consequences regarding governing equations, in Section , but as a first step, porosity of anodes and cathodes will be respectively assessed in this Section.

As stated by Liu and Chen in their work: "Porosity is defined as the ratio of the pore volume to the whole nominal volume of a porous body, and it is generally expressed as either a percentage or a decimal" [37].

Therefore, the porosity parameter in study is set to indicate how much of an electrode volume may be actually occupied by the fluids involved in the model.

**Anode** As presented in Section 4.3.1, the anode employed in the Reference Study is a graphite brush PANEX 35 50K, by ZOLTEK. Focusing on fluid dynamics studies with similar materials, the study by Logan et al. [38] adopted cylindrical graphite brushes, namely the PANEX 33 160K by ZOLTEK. The indicated porosity is 95%, and represents the closest example of graphite brushes application providing porosity. Therefore, the same porosity value has been assumed for this model.

**Cathode** The cathodes of the Reference Study are realized in SS 304 mesh sheet (mesh size 60, McMaster-Carr, Ohio). From the producer's catalogue, this mesh size is reported to feature a 31% open area, with a wire size of 0.2 mm. The study by Zhang et al. [39] features SS woven wire (plain weave) meshes of size 50 and 70, from the same manufacturer. In the study, both meshes share 0.61%. Therefore, the cathode porosity has been assumed of 60%.

### Electrodes Permeability

A concept deriving from the presence of pores, mesh, screens and in general obstacles to the fluid flow, is permeability. Permeability is defined as "the volume of a fluid of

unit viscosity passing through a unit cross section of the medium in unit time under the action of a unit pressure gradient" [40]. Furthermore, "permeability is a measure of the ease of passage of liquids or gases or specific chemicals through the material" [41]. Therefore, permeability has a crucial role in modelling the pressure jump occurring in porous media regions, i.e. the electrodes. The permeability values for anode and cathode has been assumed very roughly, especially for the anode brush. The permeability of the SS mesh screen has been assumed by following the values from the study of Yadav et al. [42], in which smaller mesh sizes are considered starting from 100#. For the 60# size of the Reference Study, a larger permeability value has been assumed, leading to a lower resistance against the flow.

**Table 5.10:** Permeability $k$ of the electrodes

| Electrode | Permeability [$m^{-2}$] |
|---|---|
| Anode | $10^{-5}$ |
| Cathode | $10^{-7}$ |

### Electrodes Electrical Conductivity

While dealing with electrodes constituted by solid materials, in this case graphite and stainless steel, electrodes' porosity influence the effective electrical conductivity. The latter may be described by the Bruggemann correction [43]:

$$\sigma_s^{eff} = (1 - \varepsilon)^{3/2} \sigma_s \tag{5.7}$$

**Table 5.11:** Effective electrical conductivity $\Sigma_s^{eff}$ of electrodes

| Electrode | Material | Conductivity [$\Omega^{-1}$ $m^{-1}$] | Porosity | Effective Conductivity [$\Omega^{-1}$ $m^{-1}$] |
|---|---|---|---|---|
| Anode | Graphite brush | 6.45 x $10^5$ [44] | 0.95 [38] | 7.21 x $10^3$ |
| Cathode | SS mesh | 1.39 x $10^7$ [45] | 0.60 [39] | 3.51 x $10^6$ |

Lastly, since Fluent allowed for only one solid electrical conductivity for scalar

$\phi_s$, representing current/electrons flow, $\sigma_s^{eff}$ was defined as 2 x $10^6$ [$\Omega^{-1}$ $m^{-1}$]

#### Electrolyte Conductivity

The electrolyte conductivity considered for the Reference Study consists in the ability of diffusing hydrogen ions, i.e. protons. It has been evaluated according to Ozgoli and Elyasi [43] with the following Equation:

$$\kappa_l^{eff} = \frac{F^2}{RT} z^2 Dc \tag{5.8}$$

**Table 5.12:** Effective conductivity of WW electrolyte

| Quantity | Value | Unit | |
|---|---|---|---|
| Temperature $T_{WW}$ | 293 | K | |
| Ionic charge $z$ | 1 | [-] | |
| Proton Diffusion coefficient $D$ | 9.31 x $10^{-9}$ | $m^2/s$ | [46] |
| Proton Concentration $C_{H^+}$ | 64.9 | $mol/m^3$ | |
| WW Effective conductivity $\kappa_l^{eff}$ | 2.3 x $10^{-3}$ | [$\Omega^{-1}m^{-1}$] | |

However, the effect of ion diffusion in the electrolyte is estimated to be negligible with respect to ion transport actuated by the WW flow.

### 5.5.3 Governing Equations

Governing equations are the means by which the phenomenon of interest will be mathematically described, so that a numerical solution can be obtained.
As introduced in Chapter 3, Fluent solves mass and momentum conservation equations for all flows [21]; moreover, additional equations have been included to properly model energy, flow and reactions of the involved chemical species and, lastly, the potential field due to the presence of charged ions and electrons.

It is important to highlight that in this Section, governing equations are reported without considering the effect of multi-phase modeling. Later in Section 5.6, multiple multi-phase models will be presented, i.e. Mixture and Eulerian, and all

the governing equations applied will be summarized once again, specifying if each equation is solved for the mixture or for each $i$ phase.

### Mass Conservation Equation

The first equation to be presented is the continuity equation, formulated accordingly to Le and Zhou [21]. As pointed out in the aforementioned assumptions (5.5.1), no transient time-dependent terms will be present in any of the equations considered. Furthermore, it can be anticipated that the source term $S_m$, reported in Table 5.13, will be equal to 0 in all the fluid regions where numerical computation takes place.

$$\nabla \cdot (\varepsilon \rho \vec{v}) = S_m \tag{5.9}$$

The influence of the porosity is taken into account only in the electrodes' regions, where the term $\varepsilon$ is different from 1.

### Momentum Conservation Equation

As for the previous Section 5.5.3, also the momentum conservation equation is reported here with the porosity coefficient $\varepsilon$, that will be meaningful, and different from 1, only in the porous regions corresponding to the electrodes' presence.

$$\nabla \cdot (\varepsilon \rho \vec{v} \vec{v}) = -\varepsilon \nabla p + \nabla(\varepsilon \mu \nabla \vec{v}) + S_v \tag{5.10}$$

Furthermore, the source term $S_v$ of the momentum conservation equation accounts for multiple phenomena depending on the region of the MEC: gravity, surface tension and viscous resistance have been considered.

- Gravity: $\rho \vec{g}$;
- External body force: $\vec{F} = -\left(D\mu v + C\frac{1}{2}\rho v_{mag} v\right)$

  takes into account viscous and inertial losses of the fluid within the porous media [42]. D and C respectively represent the viscous and inertial resistance matrices, as defined by Fluent. In this case, in the inertial term contribution

is considered negligible, due to the extremely low flow rate of the influent. Therefore, only the viscous resistance term, defined as Darcy Term, will be present, where D is defines as: $D = \frac{\varepsilon^2}{k}$;

- Surface Tension: $\chi\kappa\frac{\rho\nabla s_l}{(\rho_l+\rho_g)/2}$

  The origin of the surface tension term will be further investigated in the Multiphase Section 5.6

As for the continuity equation, the Source Terms for different regions are reported in Table 5.13.

### Energy Conservation Equation

The energy conservation equation is reported with its transport and diffusion terms, together with the source term, which assumes different values depending on the region and are reported in Table 5.13.

$$(\rho c_p)(\vec{v}\ \nabla T) = \nabla(k\nabla T) + S_T \tag{5.11}$$

In this case, $k$ represents the thermal conductivity of the fluid, while $c_p$ is the specific heat.

### Species Transport Equations

"The model predicts the local mass fraction of each species, Yi, through the solution of a convection–diffusion equation for the ith species" [29]. The equation for the $i$ species is reported, following the ANSYS FLUENT 12.0 Theory Guide [21]:

$$\nabla \cdot (\varepsilon\rho\vec{v}Y_i) = -\nabla \cdot \vec{J}_i + S_i \tag{5.12}$$

$$\text{Diffusive mass flux vector: } \vec{J}_i = -\sum_{j}^{N-1} \rho D_{ij}^{eff} \nabla \cdot Y_i \tag{5.13}$$

$$D_{ij}^{eff} = \varepsilon^{3/2} D_{ij} \tag{5.14}$$

$$\nabla \cdot (\varepsilon\rho\vec{v}Y_i) = D_{ij}^{eff}\nabla^2(\rho Y_i) + S_i \tag{5.15}$$

By modelling according to full multicomponent diffusion, the value for $i$ species in the liquid phase has been set to $10^{-9}$ [47].

The species source and sink terms $S_i$, representing the rate of consumption or production of each species, are formulated according to Faraday's Law [13]. In the Equation 5.16, it is evident the proportionality between $S_i$ and the Volumetric Current Densities $R_{an}$ and $R_{cat}$, of anode and cathode respectively.

$$S_i = \pm \frac{M_i}{n_e F} R_{an/cat} \tag{5.16}$$

Source terms for every reactor's region are specified in Table 5.13.

### Charge Conservation Equation

The electro-chemical reactions taking place inside the MEC release both electrons and hydrogen ions (protons), causing the presence of electrical current. To respectively model the flow of electrons in the solid phase [29], represented by conducting materials such as electrodes and wires, and the ions' motion in the electrolyte (WW), two scalar transport equations (5.17) and (5.18) have been defined:

$$\nabla \cdot (\sigma_s^{eff} \nabla \phi_s) = S_{\phi s} \tag{5.17}$$

$$\nabla \cdot (\dot{m}\ \phi_l - \kappa_l^{eff} \nabla \phi_l) = S_{\phi l} \tag{5.18}$$

The potential field related to $\phi_l$ has been defined only in the liquid phase, as it is generated by the presence of hydrogen ions in the electrolyte. On the contrary, the potential $\phi_s$ has been defined for the mixture, since electrons will be present inside the solid materials of electrodes, not affected by the volume fraction

Liquid phi only in liquid phase, while solid phase is present in both phases cause need it in the electrode full volume, even if the electrode is in a region of only gas phase

"The volumetric source terms $S_{\phi s}$ and $S_{\phi l}$, defined as volumetric transfer currents" [29], are summarized in Table 5.13 and have been evaluated by means of the Tafel

equation [21]:

$$R_{an} = (\zeta j_{an}^{ref}) \left( \frac{[A]}{[A_{ref}]} \right)^{\gamma_{an}} (e^{\alpha_{an} F \eta_{an}/RT}) \tag{5.19}$$

$$R_{cat} = (\zeta j_{cat}^{ref}) \left( \frac{[C]}{[C_{ref}]} \right)^{\gamma_{cat}} (e^{-\alpha_{cat} F \eta_{cat}/RT}) \tag{5.20}$$

**Overpotentials** The overpotentials appearing in Tafel equations have been defines as:

$$\eta = \phi_s - \phi_l - E_{ref} \tag{5.21}$$

$$E_{ref} = 0\,\mathrm{V} \quad \text{Anode side;} \tag{5.22}$$

$$E_{ref} = E_{oc} \quad \text{Cathode side;} \tag{5.23}$$

$$E_{cell} = \phi_{s,cat} - \phi_{s,an} \tag{5.24}$$

Lastly, the condition of Eq. 5.25 to be followed in order to respect charge conservation states that "the total current of either electrons or protons coming out from the anode catalyst layer must be equal to the total current coming into the cathode catalyst layer and must be equal to the total current caused by the proton movement through the membrane" [29]:

$$\int_{V_{an}} R_{an} dV = \int_{V_{cat}} R_{cat} dV \tag{5.25}$$

**Source Terms**

**Table 5.13:** Source terms of the governing equations [29]

| Governing equation | Volumetric source term and location of application |
|---|---|
| Conservation of mass | All regions: $S_m = 0$ |
| Conservation of momentum | $S_v = \rho\vec{g} - \frac{\mu}{k}\varepsilon^2\vec{v} + \chi\kappa\frac{\rho\nabla s_l}{(\rho_l+\rho_g)/2}$ |
| Conservation of energy | Current collectors: $S_T = \frac{I^2}{\sigma_s}$<br>Electrodes: $S_T = \frac{I^2}{\sigma_s^{eff}}$ |
| Species Transport | Anode:<br>$S_{CH_3COO^-} = -\frac{M_{CH_3COO^-}}{8F}R_{an} < 0$<br>$S_{H_2O} = -\frac{M_{H_2O}}{\frac{8}{3}F}R_{an} < 0$<br>$S_{CO_2} = \frac{M_{CO_2}}{8F}R_{an} > 0$<br><br>Cathode:<br>$S_{H_2O} = \frac{M_{H_2O}}{4F}R_{cat} > 0$<br>$S_{CO_2} = -\frac{M_{CO_2}}{8F}R_{cat} < 0$<br>$S_{CH_4} = \frac{M_{CH_4}}{8F}R_{cat} > 0$ |
| Conservation of charge | Anode:<br>$S_{\phi s} = -R_{an}; \quad S_{\phi l} = R_{an}$<br>Cathode:<br>$S_{\phi s} = R_{cat}; \quad S_{\phi l} = -R_{cat}$<br>Other regions:<br>$S_{\phi s} = 0; \quad S_{\phi l} = 0$ |

## 5.6 Multiphase modeling

The experimental setup of the Reference Study basically describes a free surface flow, with WW flowing horizontally below a gaseous methane layer, flowing upward toward two top outlets.

In order to include multiple phases in the model, i.e. one liquid phase represented by WWm and one gas phase for methane gas, Fluent provides specific models. In this Section, two of them will be presented: the Mixture and the Eulerian models. The respective properties and characteristics will be explained, to also motivate the reasons behind the choice. However, before presenting the two alternative models, common characteristics have been listed, as bubbles size assumptions, together with phases interaction parameters, i.e. surface tension and drag models.

### Surface Tension Modeling

As already presented in Section 5.5.3, the effect of surface tension in the interaction of the two phases has been modelled by adding a source term to the momentum equation. As reported by Le and Zhou [29], the pressure drop across the surface is directly proportional to the surface tension coefficient $\chi$, as in Eq. (5.26):

$$\Delta p = \chi \left( \frac{1}{R_1} + \frac{1}{R_2} \right) \tag{5.26}$$

$$\vec{F} = \chi \kappa \frac{\rho \nabla s_l}{(\rho_l + \rho_g)/2} \tag{5.27}$$

Furthermore, "R1 and R2 are the two radii, in orthogonal directions, to measure the surface curvature" [29]. Lastly, the source term related to surface tension will be reported as a volumetric force $\vec{F}$, as in Eq. 5.27, where $\kappa$ stands for the surface curvature, whose value is linked to the normal unit vector $\hat{n}$ and contact angle $\theta$.

### Bubbles Diameter

In modelling the presence of multiple phases, the gaseous phase has been set as the "second" one. Therefore, it is possible to define the size of the bubbles for methane. This is a relevant aspect since methane, as soon as it is produced on the cathode,

will form small bubbles. The aforementioned bubbles, exploiting their density 1500 times smaller than WW, will rise to the top of the reactor, basically forming a fluid-fluid interface, since a region with 100% is formed on top of a liquid one.

It is worth mentioning that the bubble diameter is involved in the definition of the particle relaxation, a parameter which is itself related to the relative (or slip) velocity concept enforced in the Mixture model, to define the difference on velocities between the two phases.

By following two studies considering the formation of methane bubbles, a rough estimation of the diameter has been assumed at 5 mm. On one side, the study of Delwiche and Hemond [48] of Methane Bubble Size Distributions in a Freshwater Lake pointed toward a distribution peak at this size. Furthermore, the CFD study by Pourtousi et al. about a "Methane bubble formation and dynamics in a rectangular bubble column" [49], produced convincing results by applying a bubble diameter size of 5 mm, too.

### Drag Model

In order to compute the momentum exchange coefficient between the two phases, a drag function has to be selected. The ANSYS FLUENT 12.0 User's Guide advises that: "The symmetric model is recommended for flows in which the secondary (dispersed) phase in one region of the domain becomes the primary (continuous) phase in another. For example, if air is injected into the bottom of a container filled halfway with water, the air is the dispersed phase in the bottom half of the container; in the top half of the container, the air is the continuous phase" [50].

### Interface Modelling

The interface modelling related to the presence of two phases has been set to "*Sharp/Dispersed*", since the two-fold nature of methane. On one side, methane gas accumulated on top may form a discrete interface with the liquid on the bottom, but at the same time, dispersed bubbles are dissolved in the continuous fluid, WW, therefore implying a dispersed modelling.

### 5.6.1 Mixture model

The Mixture model has been the first multiphase model to be adopted in this thesis. As the ANSYS FLUENT 12.0 Theory Guide states: "The mixture model is a simplified multiphase model that can be used in different ways. It can be used to model multiphase flows where the phases move at different velocities, but assume local equilibrium over short spatial length scales" [21]. The principal feature about this model is the possibility to simulate a relative (or "*slip*") velocity among the involved phases: this is achieved by the use an algebraic slip formulation. "The basic assumption of the algebraic slip mixture model is that to prescribe an algebraic relation for the relative velocity, based on the aforementioned local equilibrium between the phases should be reached over a short spatial length scale" [21]. The slip velocity definition follows the work of Mannin et al. [51].

Multiple $n$ phases may be modelled by the Mixture model, which solves momentum, continuity, and energy equations for the mixture, by a weighted average of the volume fractions. Furthermore, additional solved equations include the volume fraction equations for the secondary phases, while relative velocities depend on algebraic expressions. Bubbly flows are one of the possible applications for this model, at the condition that the gas volume fraction is low. This aspect will be critical for the model developed in this thesis.

The Mixture model represents a valid alternative to more computationally-expensive models as the full Eulerian multiphase, since it solves a reduced number of variables, especially when the secondary phases have a wide distribution.

The mixture model, uses a single-fluid approach, sharing this characteristic with the Volume-of-fluid VOF model, However, it differs from the VOF model since "mixture model allows the phases to be interpenetrating. The volume fractions $_i$ and $\alpha_j$ for a control volume can therefore be equal to any value between 0 and 1, depending on the space occupied by phase $i$ and phase $j$" [21].

One limitation of the mixture model concerning this thesis is the possibility to define only one phase as compressible ideal gas.

Here are reported the governing equations adapted for the use of the Mixture

model, with quantities with $m$ indicating mixture properties averaged between the two phases, based on volume fraction.

$$\nabla \cdot (\varepsilon \rho_m \vec{v}_m) = S_m \tag{5.28}$$

$$\rho_m = s_l \rho_l + s_g \rho_g \tag{5.29}$$

$$\vec{v}_m = \frac{s_l \rho_l \vec{v}_l + s_g \rho_g \vec{v}_g}{\rho_m} \tag{5.30}$$

$$\nabla \cdot (\varepsilon \rho \vec{v_m} \vec{v_m}) = -\varepsilon \nabla p + \nabla(\varepsilon \mu_m \nabla \vec{v_m}) + S_v \tag{5.31}$$

$$\mu_m = s_l \mu_l + (1 - s_l)\mu_g \tag{5.32}$$

$$(\rho c_p)_{eff}(\vec{v}\ \nabla T) = \nabla(k_{eff} \nabla T) + S_T \tag{5.33}$$

$$T_m = \frac{s_{\rho l} T_l + (1 - s_l)\rho_g T_g}{s_{\rho l} + (1 - s_l)\rho_g} \tag{5.34}$$

$$(\rho c_p)_m = \varepsilon \rho_f c_{p,f} + (1 - \varepsilon)\rho_s c_{p,s} \tag{5.35}$$

$$k_m = \varepsilon k_f + (1 - \varepsilon) k_s \tag{5.36}$$

### 5.6.2 Eulerian Model

The second multiphase model considered for this work is the full Eulerian model, the most complex multiphas model available on ANSYS FLUENT. According to the ANSYS FLUENT 12.0 Theory Guide [21], the fundamental features of the model are sharing a single pressure among all the phases, while solving momentum and continuity equations for each phase, as well as the other additional equations applied. Furthermore, the modification from a single phase model imply the need to "define the volume fractions ($s_i$, $s_j$, ..., $s_n$) for the multiple $n$ phases, as well as mechanisms for the exchange of momentum, heat, and mass between the phases" [52]. Furthermore, "applications of the Eulerian multiphase model include bubble columns, risers, particle suspension, and fluidized beds" [21].

### 5.6.3 Model Comparisons

The selection of a multiphase model starts by determining the flow regime involved, in order to follow the relative guidelines associated to the simulated flow.

As stated in ANSYS FLUENT 12.0 Theory Guide, "the VOF model is appropriate for stratified or free-surface flows, and the mixture and Eulerian models are appropriate for flows in which the phases mix or separate and/or dispersed-phase volume fractions exceed 10%" [53].

Therefore both models are indicated for the simulation of bubbly flows. Furthermore, in both models "the phases are treated as interpenetrating continua" [21].

At last, three criteria for choosing between mixture and the Eulerian model are indicated, quoting from the ANSYS FLUENT 12.0 Theory Guide:

- If there is a wide distribution of the dispersed phases (i.e., if the particles vary in size and the largest particles do not separate from the primary flow field), the mixture model may be preferable (i.e., less computationally expensive). If the dispersed phases are concentrated just in portions of the domain, you should use the Eulerian model instead [54].
- If interphase drag laws that are applicable to your system are available, the Eulerian model can usually provide more accurate results than the mixture model. Even though you can apply the same drag laws to the mixture model: if the interphase drag laws are unknown or their applicability to your system is questionable, the mixture model may be a better choice [54].
- To solve a simpler problem, which requires less computational effort, the mixture model may be a better option, since it solves a smaller number of equations than the Eulerian model. If accuracy is more important than computational effort, the Eulerian model is a better choice. Keep in mind, however, that the complexity of the Eulerian

model can make it less computationally stable than the mixture model [54].

## 5.7 Boundary Conditions

**Table 5.14:** Boundary Conditions

| Location | Boundary Condition |
|---|---|
| Inlet of WW | $\dot{m}_{in} = \dot{m}_{WW}$; $Y_{CH_3COO^-} = Y_{CH_3COO^-,in}$ $T_{in} = T_{WW}$ |
| Outlet of the liquid phase | $p = p_{atm}$ |
| Outlet of the gas phase | To be defined |
| Anode terminal | $\phi_s = 0$ |
| Cathode terminal | $\phi_s = E_{cell}$ |
| External boundaries | No-slip condition; Adiabatic = No heat flux; |

### 5.7.1 Initial Solution

The parameters set for the initial solution, i.e. the parameters upon which the first iteration will be based on, are reported here:

**Table 5.15:** Initial Conditions

| Location | Initial Condition | Value |
|---|---|---|
| Inlet surface | Inlet x-axis velocity | $1.39\,\text{x}\,10^{-4}$ m s$^{-}$1 |
| | Acetate Mass fraction | $0.001\,\text{g L}^{-1}$ |
| | Inlet Gauge Pressure | 0 Pa |
| | Temperature | 293 K |
| | Volume Fraction | 0 |
| | $\phi_s$ Potential | 0 V |
| | $\phi_l$ Potential | 0 V |

## 5.8 Solution methods

The numerical method chosen for the solution of the CFD is the Pressure-Based solver available in FLUENT. The ANSYS FLUENT 12.0 Theory Guide states that "the pressure-based solver employs an algorithm which belongs to a general class of methods called the projection method, wherein the constraint of mass conservation (continuity) of the velocity field is achieved by solving a pressure (or pressure correction) equation. The pressure equation is derived from the continuity and the momentum equations in such a way that the velocity field, corrected by the pressure, satisfies the continuity" [21]. Due to the non-linearity of the governing equations coupled to each other, an iterative procedure is required in order to converge to solution.

**Table 5.16:** Discretization schemes

| Pressure-Velocity Coupling | SIMPLEC<br>Skewness Correction 1 |
|---|---|
| Spatial Discretization: | |
| Gradient | Least Squares Cells Based |
| Pressure | PRESTO! |
| Momentum | First Order Upwind |
| Volume Fraction | Implicit |
| Energy | First Order Upwind |
| User Scalar $\phi_s$ | QUICK |
| User Scalar $\phi_l$ | QUICK |
| Liquid phase Species | QUICK |
| Gas phase Species | QUICK |

ANSYS FLUENT is based on a FVM, which discretizes unknowns in the computational nodes of the mesh grid. However, the convection terms of the governing equations involve surface integrals implying that face values of the unknowns have to be interpolated from the cell node values. The task is accomplished by an *upwind* scheme, which is based on deriving the face value from the cell "*upstream*" with respect to the normal velocity; FLUENT offers a wide variety of these schemes. On the contrary, diffusion terms feature second-order accuracy by being

central-differenced [21].

**Gradient** Also regarding the gradient, a method for its calculation is needed due to its importance in the numerical method. "The gradient $\nabla\phi$ of a given variable $\phi$ is used to discretize the convection and diffusion terms in the flow conservation equations" [21].

**Momentum** For the momentum conservation equation in a multiflow setup, the advised discretization scheme advised is the first order.

**Pressure-Velocity Coupling** Pressure-velocity coupling is intended to derive an additional condition for pressure by reformatting the continuity equation. Among the available schemes, SIMPLE (and SIMPLEC) algorithm uses a relationship between velocity and pressure corrections to enforce mass conservation and to obtain the pressure field, as described in the ANSYS FLUENT Theory Guide:

> For relatively uncomplicated problems (laminar flows with no additional models activated) in which convergence is limited by the pressure-velocity coupling, you can often obtain a converged solution more quickly using SIMPLEC. In some problems, however, increasing the pressure-correction under-relaxation to 1.0 can lead to instability due to high mesh skewness. For such cases, you will need to use one or more skewness correction schemes, use a slightly more conservative under-relaxation value (up to 0.7). However, SIMPLEC will improve convergence only if it is being limited by the pressure-velocity coupling. Often it will be one of the additional modeling parameters that limits convergence; in this case, SIMPLE and SIMPLEC will give similar convergence rates [55].

The SIMPLEC procedure is similar to the SIMPLE, and the only difference consists in the expression for the face flux correction.

Furthermore, for meshes involving a certain level of skewness, the ANSYS FLUENT Theory Guide states:

The approximate relationship between the correction of mass flux at the cell face and the difference of the pressure corrections at the adjacent cells is very rough. After the initial solution of the pressure-correction equation, the pressure-correction gradient is recalculated and used to update the mass flux corrections. This process, which is referred to as "skewness correction", significantly reduces convergence difficulties associated with highly distorted meshes. The SIMPLEC skewness correction allows ANSYS FLUENT to obtain a solution on a highly skewed mesh in approximately the same number of iterations as required for a more orthogonal mesh [56].

**Pressure Interpolation Scheme** For flows through porous media, the use PRESTO! is advised

**Volume Fraction** Eulerian multiphase model, select First Order Upwind, QUICK, or Modified HRIC as the Volume Fraction Spatial Discretization

**QUICK** For the other governing equations, the chosen scheme is QUICK. Its use is recommended for "quadrilateral and hexahedral meshes, where unique upstream and downstream faces and cells can be identified. The QUICK scheme will typically be more accurate on structured meshes aligned with the flow direction" [21].

**Warped-Face Gradient Correction** In order to further improve gradient accuracy, a Warped-Face Gradient Correction (WFGC) method is enabled, which "corrects gradient accuracy degradation due to very high aspect ratio cells, non-flat faced cells in the boundary layers, and any highly deformed cells with cell centroid outside of the control volume" [57]

### 5.8.1 Under-Relaxation

Relaxation factors are able to improve the stability of the solution by controlling its under relaxation, practically limiting how much a variable can be altered with

respect to the previous iteration. In this study, and in general, they represent a crucial feature in order to avoid the divergence of the solution in the first iterations. An relaxation factor may have a value between 0 and 1, with $0.3 < \text{RF} < 0.7$ usually being a good compromise between solution stability and solution time [58]. The adopted relaxation factors are reported in the following Table.

**Table 5.17:** Relaxation factor

| Quantity | Relaxation factor |
|---|---|
| Pressure | 0.3 |
| Density | 0.5 |
| Body Forces | 1 |
| Momentum | 0.5 |
| Vaporization mass | 1 |
| Slip velocity | 0.1 |
| Volume Fraction | 0.5 |
| Energy | 0.2 |
| User Scalar $\phi_s$ | 0.01 to 0.9 |
| User Scalar $\phi_l$ | 0.01 to 0.9 |
| Liquid phase Species | 0.9 |
| Gas phase Species | 1 |

## 5.9 Solution Strategy

The two objectives presented in Section 5.1 have been addressed separately, even if they complete each other composing the final model. As the electrochemical modeling based on electric field potential had a very slow convergence, once convergence was achieved and species rates matched the experimental data, attempts to model Objective 2 were performed with constant-rate source and sink terms, to reduce the computational cost.

### 5.9.1 Objective 1: Electrochemical

In order to achieve a first partial solution, focusing on the electrochemical consumption and production of species as explained in Section 5.1, a particularly

stringent boundary condition was needed to be assumed. The two gas outlets located on the top of the reactor were treated as "*walls*" boundary conditions, therefore temporarily simulating a flow with 1 inlet and only 1 outlet. At the same time, the multiphase model describing the mechanism of methane being no longer dissolved in WW and entering the gas phase, by means of the Fluent "Mass transfer Mechanism", was temporarily disable, i.e. with null rate of transfer.

### 5.9.2 Objective 2: Multiple phases

The model being developed in this study focuses also on a second objective, presented in Section 5.1, which is the simulation of liquid-gas phases interactions. Due to the complexity of such task, several methods are advised by the ANSYS FLUENT 12.0 Theory Guide [21] in order to obtain a better convergence behaviour. The steps taken to obtain an initial solution, before solving the Eulerian multiphase model are stated by ANSYS FLUENT 12.0 Theory Guide:

- Set up and solve the problem using the mixture model (with slip velocities) instead of the Eulerian model. You can then enable the Eulerian model, complete the setup, and continue the calculation using the mixture-model solution as a starting point.

- Set up the Eulerian multiphase calculation as usual, but compute the flow for only the primary phase. To do this, deselect Volume Fraction in the Equations list in the Equations dialog box. Once you have obtained an initial solution for the primary phase, turn the volume fraction equations back on and continue the calculation for all phases.

- For problems involving a free surface or sharp interfaces between the phases, it is recommended that you use the symmetric drag law. [21]

### 5.9.3 Alternative strategy: Patching

As the numerical solution is being computed, convergence to a gas volume fraction equal to 1 in the headspace, i.e. 100% gas phase and absence of liquid WW phase, may take too long. Therefore, a method may be to implement "Patching" by imposing a volume fraction equal 1 in the appropriate top region of the reactor. However, instabilities in the solution may arise so this action is better to be couple with under relaxation parameters.

## 5.10 Convergence

The criteria for convergence was based on the threshold for residuals, set at $10-6$. However, the variables of interest were monitored, i.e. species mass fractions, electric potentials, volumetric currents, to assess is their value had stabilized converging even before all the residuals were below the set threshold.

# Chapter 6

# Numerical Simulation Results

In this chapter the numerical simulation results are presented, divided between the two main Objectives pursued in this work, as presented in the previous Chapter. The simulation has been performed by applying the developed model with the input parameters of the Reference Study.

In the visualization of the numerical solution, two x-y planes have adopted for side views: the first plane is the symmetry plane, splitting in half the reactor along x-y plane. Instead, the second plane is located between the symmetry plane and the side of the reactor, sectioning the electrodes, that otherwise would not be visible in the symmetry plane. Figure 6.1 reports a view of the second plane sectioning the electrodes.

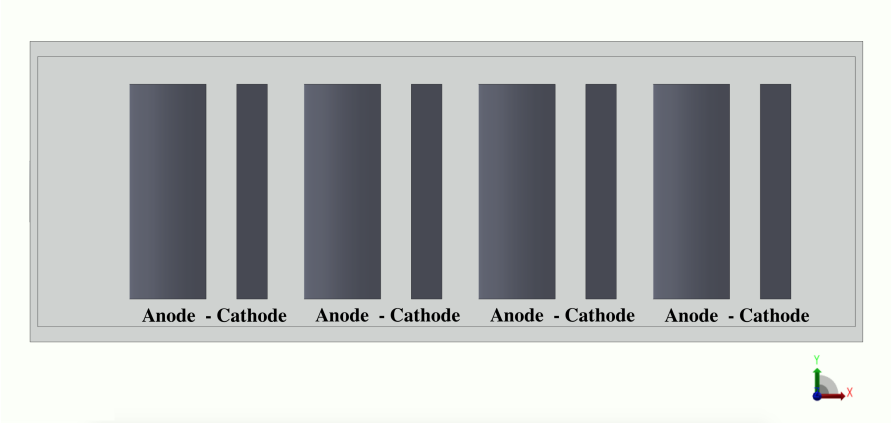


**Figure 6.1:** Section of the lateral plane used for the visualization of the solution. All the graphic have been produced in this side plane, except as noted.

### Mass Imbalance

The first graphic of the solution being reported is based on the mass imbalance of each mesh element present in the symmetry plane. The difference among entering and exiting fluxes is computed and reported, according to the scale. All values are in the same order of magnitude of $10^{-17}$, therefore confirming the quality of the mesh.

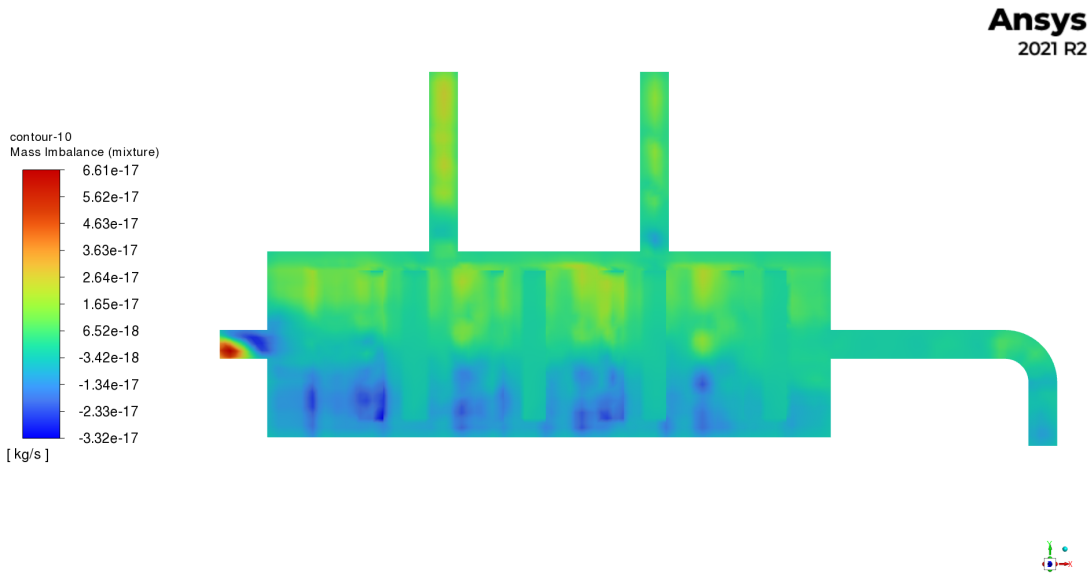


**Figure 6.2:** Mass Imbalance for mesh cells in central x-y plane

### Reynolds Number

By analyzing the Reynolds number for both plane, the presence of porous electrodes creating a viscous resistance to the flow is clear. Especially cathode, with lower porosity and lower permeability are responsible for the increase in the Reynolds number in the area adjacent to the electrodes.

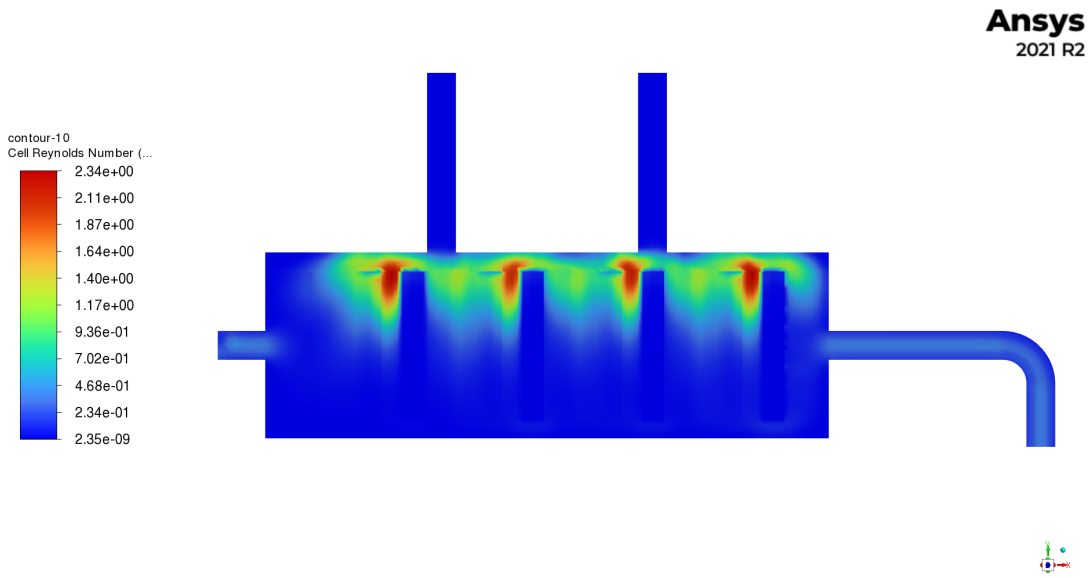


**Figure 6.3:** Reynolds Number for mesh elements in central x-y plane

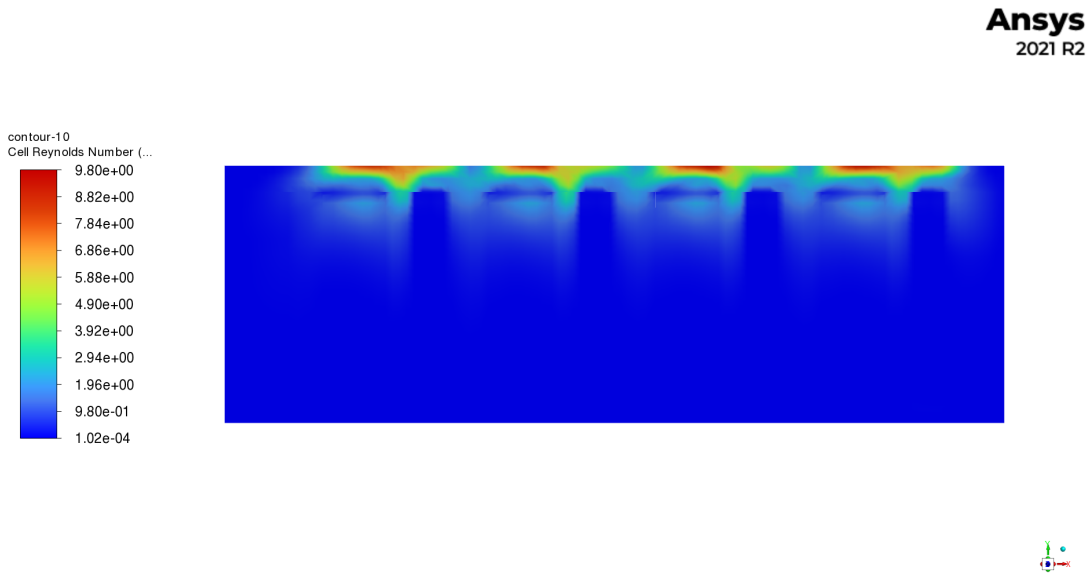


**Figure 6.4:** Reynolds Number for mesh elements

## 6.1 Objective 1

The output parameters monitored with respect to Objective 1 focus on species consumption and production, i.e. COD removal and methane production rate respectively, and on the daily averaged current through electrode pairs. The reference day selected from the experimental data is referred to day 17, to which the numerical solution will be compared with.

### 6.1.1 Species

Consumed and produced species are directly proportional to species source and sink terms, which are ultimately influenced by volumetric current terms $R_{an}$ and $R_{cat}$, reported later in Section 6.1.3. Therefore, the numerical results of CFD-computed COD removal and methane output are ultimately dependent from Volumetric Current terms.

#### COD Removal

The first CFD result to be compared with experimental data from day 17 is the amount of COD removal, which is defined as the difference in acetate concentration between the influent substrate and the liquid outlet, multiplied by the acetic acid COD equivalent.

$$\Delta\text{COD} = 1.07 \cdot (C_{Acetate,in} - C_{Acetate,out}) \tag{6.1}$$

**Table 6.1:** Numerical results for Acetate Mass fraction at inlet and outlet; Numerical vs. Experimental COD removal

| | CFD | | Experimental | Error |
|---|---|---|---|---|
| $C_{Acetate,in}$ | $C_{Acetate,out}$ [g/L] | $\Delta\text{COD}_{CFD}$ | $\Delta\text{COD}_{Experimental}$ [g/L] | % |
| 1 | 0.534 | 0.498 | 0.48 | 3.75 |


**Figure 6.5:** Acetate $CH_3COO^-$ Mass Fraction

From this Figure, it is visible that the flow at the bottom carries a higher concentration of acetate, because the wastewater is not passing through anode and therefore acetate is not being consumed.

### Methane

Secondarily, the methane output of the numerical solution has been compared to the value obtained in the Reference Study, always referring to day 17. On this day, the MEC output consisted of only methane gas, in the amount of 0.24 L, with no hydrogen gas or carbon dioxide being collected from the gas outlets. However, in the present CFD-model setup it was not possible to simulate methane entering the gas phase and rising to the top outlet, which instead where treated as walls. Therefore, the data indicating the methane outflow refers to the amount of methane produced by the cathodes and remaining in the liquid flow even if not realistically feasible due to the threshold of water solubility. The methane then exits and is measured from the liquid outlet, but still provides valuable data indicating that cathode production exists and is in line with the expected output.

**Table 6.2:** Volumetric daily production of Methane: Numerical vs. Experimental results

| | CFD | Experimental | Error [%] |
|---|---|---|---|
| Methane [L/day] | 0.234 | 0.24 | 2.50 |

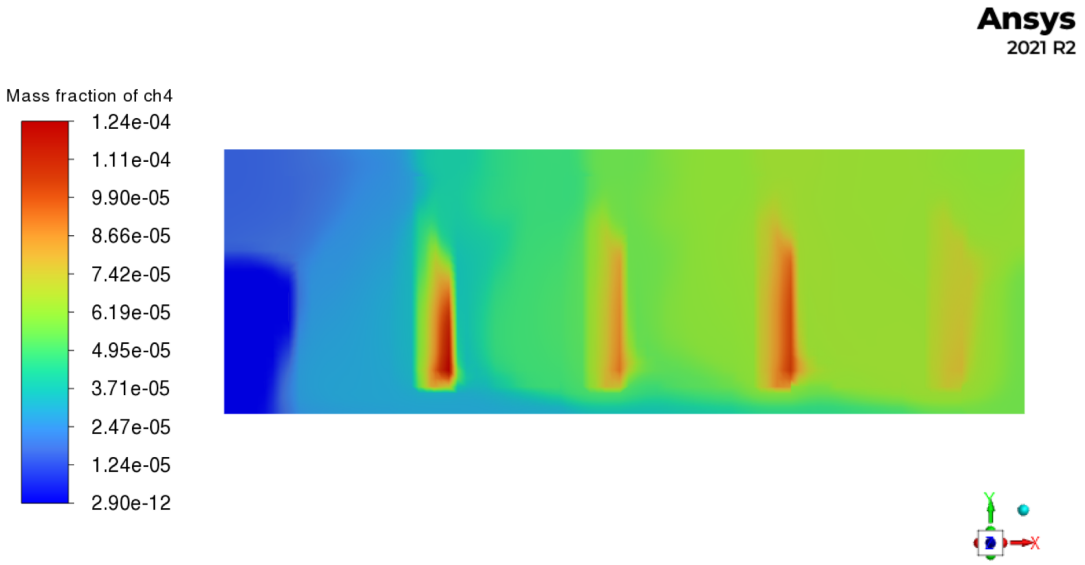


**Figure 6.6:** Methane $CH_4$ Mass Fraction

The concentration of methane is clearly higher in the regions of the cathode. This is an encouraging result, showing that methane is being produced. However, a future step of the simulation will be the conversion of methane into gas phase, rising at the top due to the difference of density.

### 6.1.2 Current

The third numerical result to be compared with experimental data is the daily averaged current relative to one single electrode pair, whose value has been interpolated from Figure 4.5. As the numerical solution relies on volumetric current values, the current value has been obtained following Equation 6.2 and 6.3, for anode and cathode regions respectively, by multiplying volumetric current with

the electrode volume. Furthermore, Equation 6.4 expresses required condition that the total current coming into the cathode stainless steel mesh must be equal to the total current caused by the proton movement in the electrolyte, adapting what is expressed in the work from Le and Zhou [29].

$$I_{an} = R_{an} \cdot V_{an} \tag{6.2}$$

$$I_{cat} = R_{cat} \cdot V_{cat} \tag{6.3}$$

$$\int_{V_{an}} R_{an} dV = \int_{V_{cat}} R_{cat} dV \tag{6.4}$$

**Table 6.3:** Current of a single electrode pair: Numerical vs. Experimental results

| | Anode | Cathode | Experimental | Error |
|---|---|---|---|---|
| Current [A] | 0.02168 | 0.02166 | 0.022 | 1.5 % |

### 6.1.3 Numerical vs. Theoretical Results

In the following comparison, the difference among the numerical results and the theoretical data has been estimated. However, it does not fully represent an error, since the theoretical data have been calculated from the available data of the Reference Study and does not play a role toward the model validation. The difference visible in these electrochemical data could be motivated by the arbitrary nature of the reference current and concentration terms present in the Tafel Equation.

**Table 6.4:** Comparison of numerical and theoretical electrochemical paramters

| Quantity | CFD | Theoretical | Unit | Difference |
|---|---|---|---|---|
| $R_{an}$ | 316 | 297 | A $m^{-3}$ | 6.3% |
| Sink Acetate | -2.43 x $10^{-5}$ | -2.27 x $10^{-5}$ | kg $m^{-3}$ $s^{-1}$ | |
| Source Carbon Dioxide | 1.80 x $10^{-5}$ | 1.69 x $10^{-5}$ | kg $m^{-3}$ $s^{-1}$ | |
| $R_{cat}$ | 334 | 314 | A $m^{-3}$ | 6.0% |
| Sink Carbon Dioxide | -1.90 x $10^{-5}$ | -1.79 x $10^{-5}$ | kg $m^{-3}$ $s^{-1}$ | |
| Source Methane $CO_2$ Reduction | 1.04 x $10^{-6}$ | 9.78 x $10^{-7}$ | kg $m^{-3}$ $s^{-1}$ | |

### 6.1.4 Visualization

In this Section, the graphics relative to: species terms; volumetric currents; overpotentials and electric potential fields have been reported. The global scale of the graphics does not always allow to appreciate smaller local variations, as in some regions the values are much greater, overshadowing the other variations present. Each graph is reported with its own color scale on the left, while the frame of reference is specified on the right. Furthermore, even if the whole plane is reported in the graphic, species and current terms are only active in the regions of the electrodes.

#### Species Terms

The species terms visualized on the plane sectioning the electrodes have precisely the aim to show the achieved intensity of source and sink terms, caused by the electrochemistry principles modelled by governing equations. Respectively two graphics have been reported for the anode and for the cathode, while the modelling of the methane formed acetoclasitcally from methane has been considered not of interest for the study.


**Figure 6.7:** Acetate $CH_3COO^-$ Sink Term, active at the Anode


**Figure 6.8:** Carbon Dioxide $CO_2$ Sink Term, active at the Anode


**Figure 6.9:** Carbon Dioxide $CO_2$ Sink Term, active at the Cathode

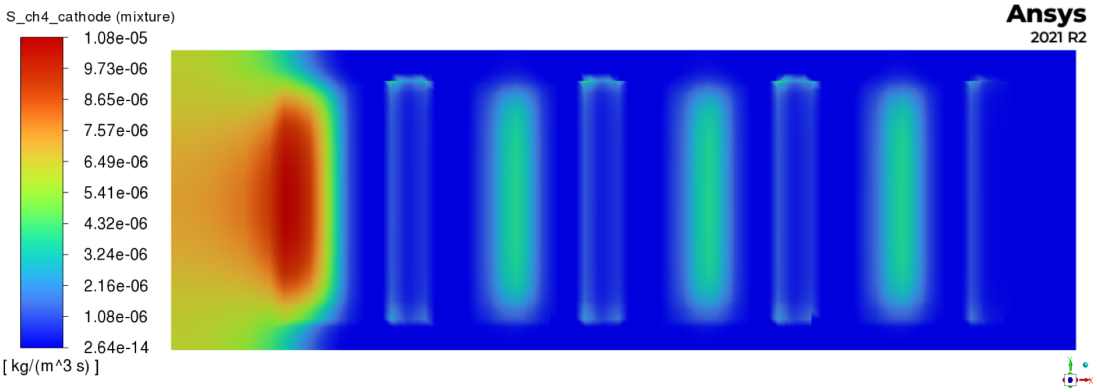


**Figure 6.10:** Methane $CH_4$ Source Term, active at the Cathode

### Volumetric Currents $R_{an}$ and $R_{cat}$

The volumetric currents are the terms upon which species terms are based on according to Faraday's law, therefore their graphics understandably follow the same trend seen before for the involved species.


**Figure 6.11:** Anode Volumetric Current $R_{an}$

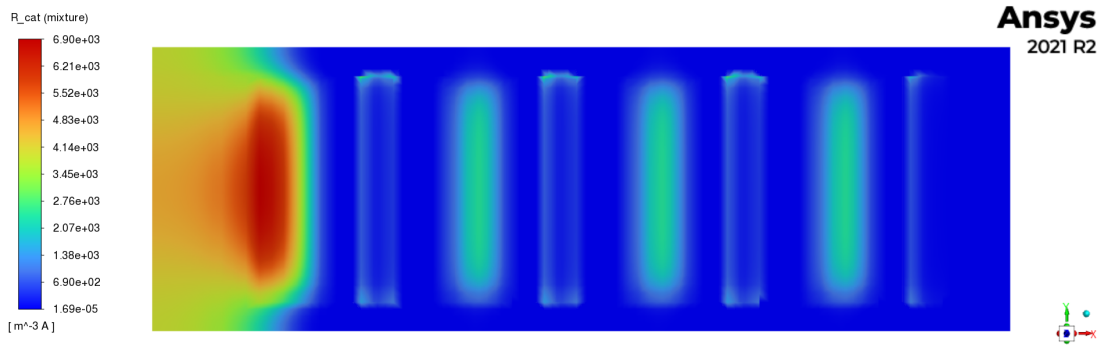


**Figure 6.12:** Cathode Volumetric Current $R_{cat}$

### Overpotentials $\eta_{an}$ and $\eta_{cat}$

The overpotentials have been defined as according to Eq. 5.21. Therefore they represent the difference between the two potential fields, while the reference voltage varies from anode where is 0 V to the cathode where is the set open circuit potential. Since their difference is represented by a constant value, their trends will be similar.

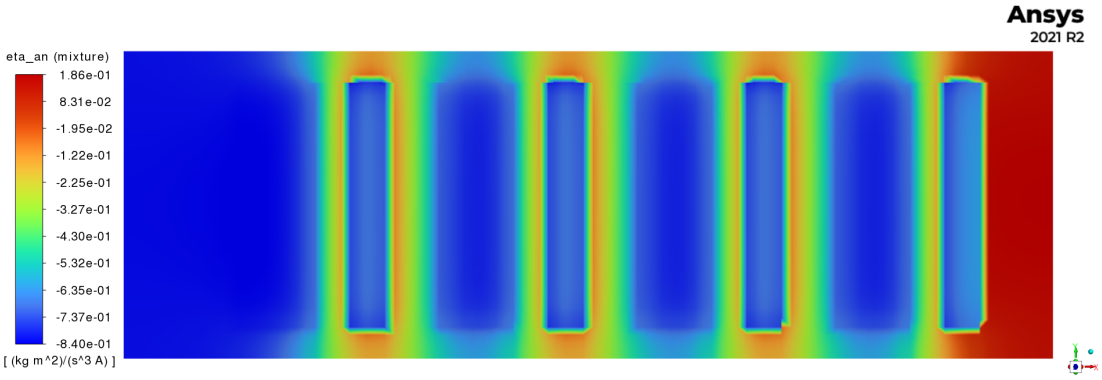


**Figure 6.13:** Anode Overpotential $\eta_{an}$

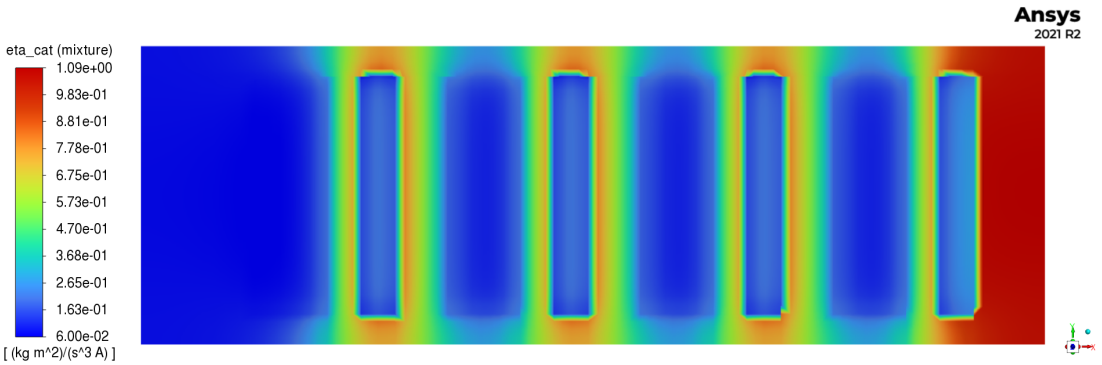


**Figure 6.14:** Cathode Overpotential $\eta_{cat}$

### Electric Potential Fields $\phi_s$ and $\phi_l$

The electric potential fields are visualized in this Section. Figure 6.15 clearly shows the potentials applied to the electron-conducting materials of the electrodes. The anode is set to 0 V, while the cathode features a negative voltage as predicted. The graphic does not include liquid area. On the contrary, Figure 6.16 shows the trend of the potential in the liquid electrolyte, due to the presence of protons released at the anode and consumed at the cathode.

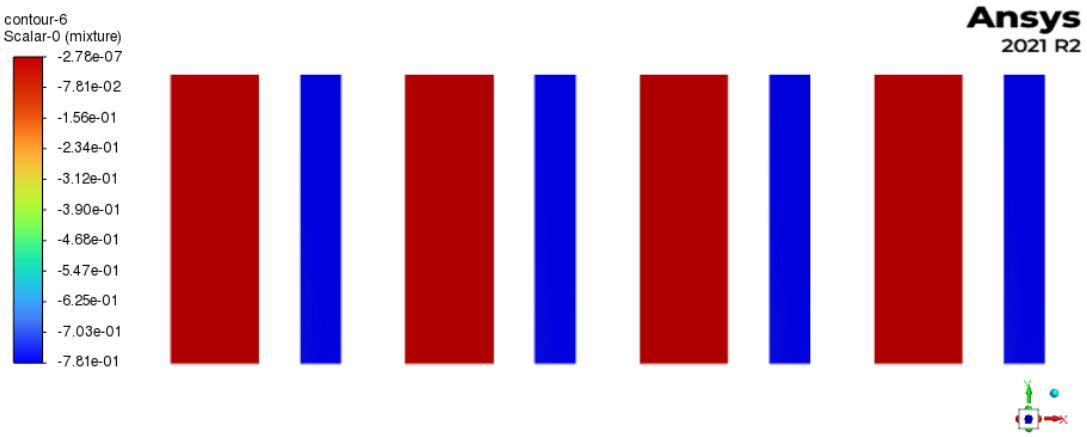


**Figure 6.15:** Electric Potential $\phi_s$ scalar field

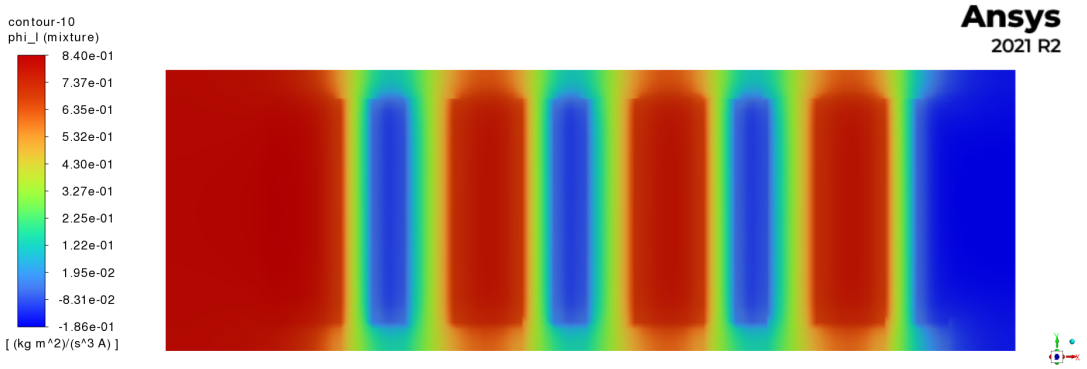


**Figure 6.16:** Electric Potential $\phi_l$ scalar field

## 6.2 Residuals

The residual of the governing equations are reported in the Figure below, relative to the solution of the full model for Objective One, as visible by the presence of "uds-0" and "usd-1". These two therms represent the Charge conservation equations, based on the creation of two scalar potential fields $\phi_s$ and $\phi_l$. Not all residuals reached a value lower than the threshold set at $10^{-6}$. However, the variables of interest were able to stabilize, confirming the found convergence of the solution.

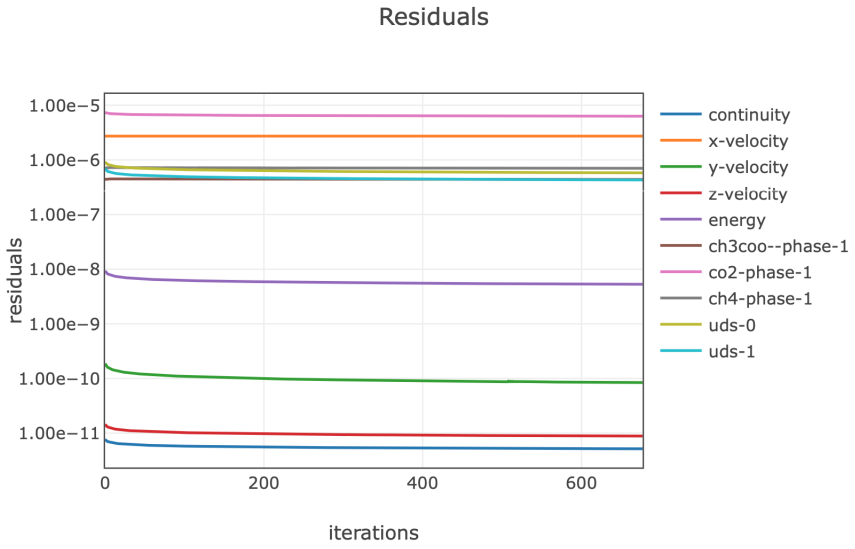


**Figure 6.17:** Residuals of the solution, versus number of iterations

### 6.2.1 Objective 2

The second main objective of this model, i.e. the simulation of rising bubbles of methane from the cathode, accumulating in the top headspace of the reactor, has not been successful. The convergence of the solution was not achieved, even by applying the solution strategy listed in Section 5.9.2. Following Fluent *Multiphase* modelling, a mass transfer was set between the two phases for the methane species, meaning that as soon as methane was formed at the cathode, the model converted its phase to gaseous. However, the volume fractions achieved in all the regions of the reactor did not match the attended theoretical results: in the upper region of approximately 0.3 L, the volume fraction should have converged to 1, equalling to 100% of gas phase. However, also when applying a "*Patch*" in this upper region by imposing a volume fraction equal to 1, the solution quickly diverged, even with a strong under-relaxation.

The Figure 6.18 reported below represents a later-diverged solution, which may approximate well the expected results. By analyzing the image bottom-up, it possible to notice that at the floor of the reactor the volume fraction is close to 0, while in the electrode regions increases around 0.2, in line with the expected presence of methane gas rising to the top. Lastly, at the top of the reactor is visible a quick transition to more than 80% of gas phase, while is the two top ducts the volume fraction is 1.

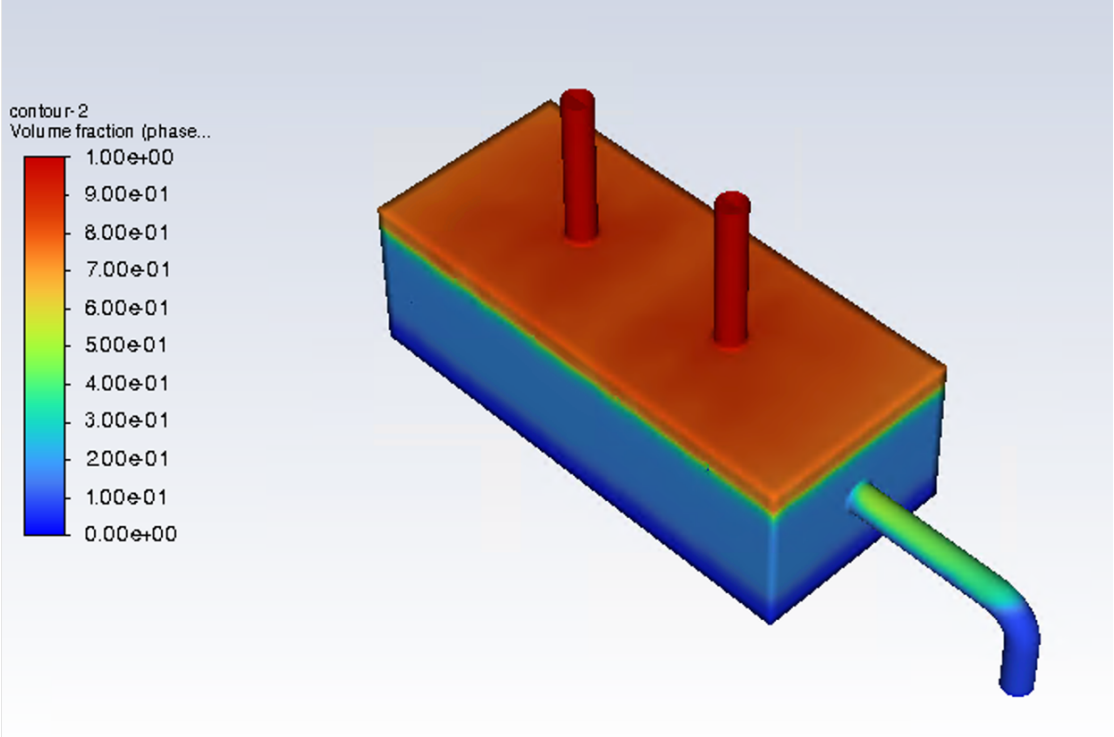


**Figure 6.18:** Isometric view of the expected Gas-Phase Volume Fraction

## 6.3 Total time required for solution

The solution of the CFD model required between 2 and 5 hours when modelling the electrochemical parameters, fundamental toward Objective One. However, by setting as constant those parameters and solving only of multiphase modeling, the target of Objective Two, the solution proceeded much faster, although it did not converge and soon showed stability problems.

# Chapter 7

# Conclusions and future directions

In this Master's thesis, the CFD model of a methane-producing MEC has been developed. Firstly, the theory principles behind electrochemical methanogenesis have been presented, along with the basics of the FVM applied to CFD modelling. Subsequently, a Reference Study has been selected in order to perform the validation of the model, by means of the available experimental data.

The model has been developed following the available literature on the subject, especially relying on the reactors realized respectively by Rader and Logan; and Nelabhotla and Dinamarca. However, various degrees of adaptation have been performed, by means of assumptions. On a geometrical level, this translated in the simplification of the shapes of the electrodes, in order to work with a more homogeneous and less computationally-heavy mesh, featuring elements with dimensions in the order of magnitude of millimeters rather than microns.

Furthermore, the design of the electrochemical reactions taking place inside the reactor represents a challenge since the control of microbial populations, responsible for different methane pathways, still has not been fully mastered. As presented in the literature, the presence of methanogens was firstly addressed as a problem, since it interfered with hydrogen gas production. However, the tenacity of these

populations against wash-off, coupled to the advantages of dealing with methane rather than hydrogen as a power vector, intensified the research upon electro-methanogenesis. The state-of-the-art regarding methane-producing MECs may be represented by work of Nelabhotla and Dinamarca, quantifying around 15% the potential increase of methane production due to the exploitation of hydrogenotropic pathway.

This percentage of hydrogenotropic methane was assumed in the model developed in this thesis, which was fitted to match with experimental conditions of the reactor by Rader and Logan. The selection of their study was not accidental: the design of the reactor ideally allowed for a neat distinction between the two phases present simultaneously inside the cell. On one hand, wastewater crosses the reactor by means of an horizontal flow; at the same time, the gas phase produced by means of acetoclastic methanogens and electrochemistry rises vertically to the top. Furthermore, the characteristics of a single-chamber continuous-flow cell were all present, coupled with a multi-electrode layout.

The results of the simulation allowed to partially validate the developed model. The first objective of the model consisting in the modelling of the electrochemical parameters was met, even if by enforcing a temporary wall BC on the gas outlets which will later need to be removed. The imposition of an electrical potential difference at the solid current conductors of each pair of electrodes induced a flow of electrons, modelled by a electric potential field in the solid phase. A second potential field in the liquid phase was due to protons. The two potential fields were responsible for the presence of volumetric currents, which have been modelled according to Tafel Equation, in the regions corresponding to the electrodes. This ultimately allowed to correlate the applied potential to the rates at which species have been consumed and produced inside the cell, achieving the same COD removal and methane production of the Reference Study, with the same observed current.

On the other hand, the second objective consisting in the effective modelling of the interaction between liquid and gas phase was not fully met. The solution was quick to diverge with any of the methods applied. A strong initial relaxation

did not allow to reach converge, even when coupled with a sequential solution strategy composed of multiples steps. However, there is reason to be confident on the physical parameters set for the multiphase modelling, therefore ascribing the failure of converging to a solution to the mathematical method applied.

Lastly, the Grid Convergence Study yielded a successful outcome, showing an increased convergence of the results when the number of mesh elements was augmented.

To summarize, it may be argued that this thesis proved the feasibility to develop an initial CFD model focused on the electrochemical principles present inside a MEC. However, further investigation is strongly needed to fully achieve a convergence of the model, especially regarding the simulation of multiple phases, before being able to exploit this tool for the optimization of a reactor.

The difficulties encountered in the development of the model may be partially explained by considering the relatively new nature of this technology. As a matter of fact, CFD literature studies regarding conventional fuel cells and electrolysis cells are vastly more numerous. This model itself has been largely based on the governing equations and guidelines existing for FC and EC, which usually do not feature liquid flows as the WW.

Lastly, as a future development this thesis would advise to conduct a set of experiments on a new reactor prototype, already designed with the intention of developing a CFD model, as in the work of El Ibrahimi et al. [28]. This would allow to:

- Reduce the uncertainty of the chemical reactions happening inside the reactor, which greatly influence the confidence in the model. The catalyzing action carried out by hydrogenotropic methanogens would benefit from additional characterization. Especially, focusing on the relationship existing among HRT, microbial film thickness and the achievable catalyzing properties, which in the present model has been taken as constants not truly influenced by the change of working conditions, would benefit the reliability of the study. Species source and sink terms may be based not only on electrochemical properties as of now,

but on additional microbial parameters, which has to be investigated further;

- Carefully characterize the permeability of the adopted electrodes with experimental testing. The pressure jump caused by the porous media would be modeled more accurately;

- Determine experimentally the Reference Currents and Reference Concentrations which are important parameters influencing the outcome of the Tafel Equation.

# Appendix A

# Model Development

## A.1 Geometry

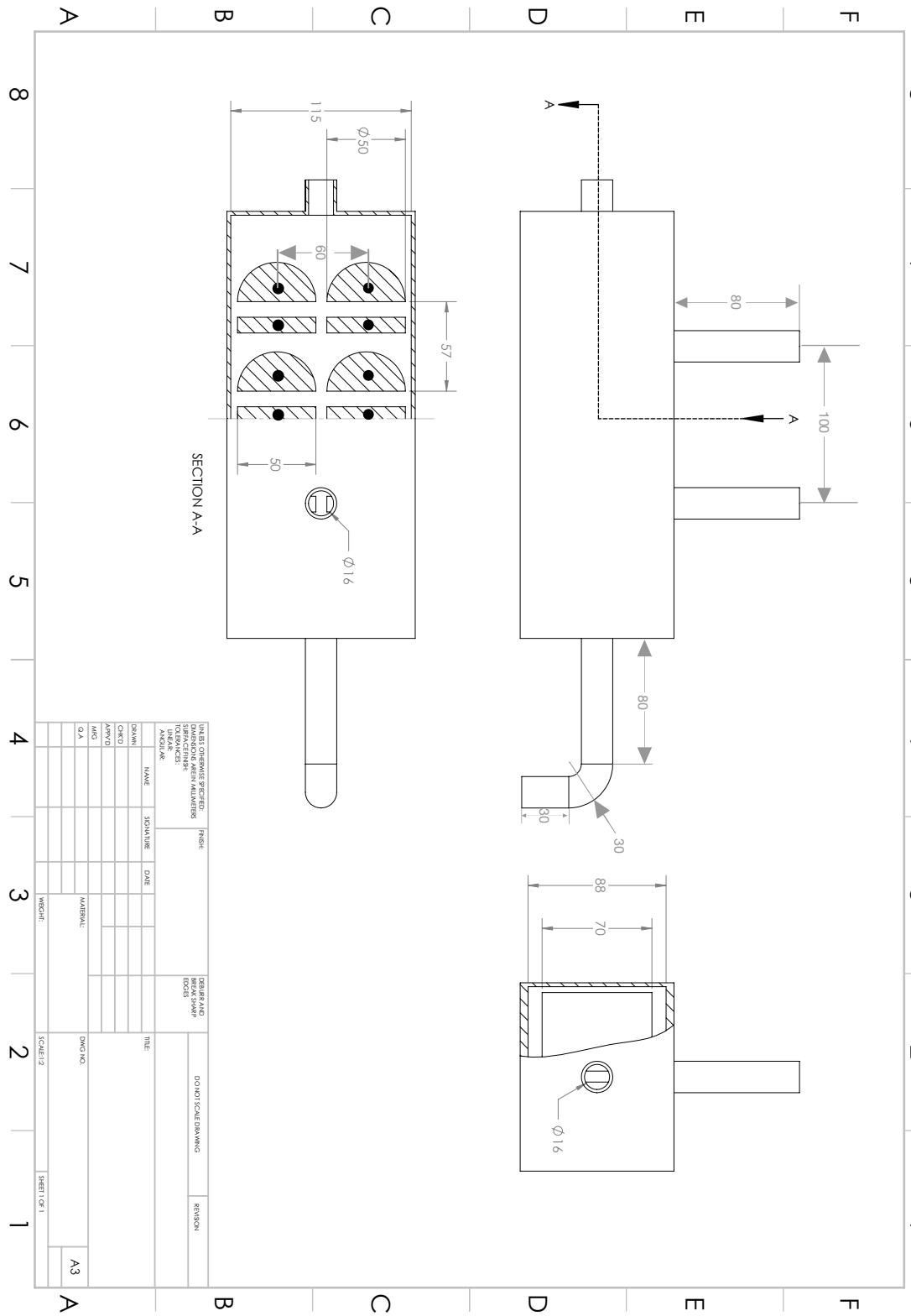


**Figure A.1:** Technical drawing of the simplified reactor geometry

# Bibliography


[1] Shaoan Cheng, Defeng Xing, Douglas F. Call, and Bruce E. Logan. «Direct Biological Conversion of Electrical Current into Methane by Electromethanogenesis». In: *Environmental Science & Technology* 43.10 (2009), pp. 3953–3958. DOI: 10.1021/es803531g. URL: https://doi.org/10.1021/es803531g (cit. on pp. 2, 5–7, 9, 12, 14, 15, 17).

[2] Anirudh Bhanu Teja Nelabhotla and Carlos Dinamarca. «Bioelectrochemical CO2 Reduction to Methane: MES Integration in Biogas Production Processes». In: *Applied Sciences* 9.1056 (2019) (cit. on pp. 2, 7, 9, 11–13, 16, 17, 26, 35).

[3] Mahedi Hasan Ibna Saif. *Pilot Design of a Bioelectrochemical MES Wastewater Reactor*. Faculty of Technology, Natural sciences and Maritime Sciences Campus Porsgrunn, 2020 (cit. on p. 2).

[4] Geoffrey K Rader and Bruce E. Logan. «Multi-electrode continuous flow microbial electrolysis cell for biogas production from acetate». In: *International Journal of Hydrogen Energy* 35.17 (2010), pp. 8848–8854 (cit. on pp. 3, 13, 16, 25, 27–32, 35, 40, 41).

[5] R. Blasco-Gómez, P. Batlle-Vilanova, M. Villano, M. Dolors Balaguer, J. Colprim, and S. Puig. «On the Edge of Research and Technological Application: A Critical Review of Electromethanogenesis». In: *International Journal of Molecular Sciences* 18.4 (2017). URL: https://www.mdpi.com/1422-0067/18/4/874 (cit. on pp. 5, 6, 9, 16).

[6] Kengo Sasaki, Masahiko Morita, Norio Matsumoto, Daisuke Sasaki, Shin-ichi Hirano, Naoya Ohmura, and Yasuo Igarashi. «Construction of hydrogen fermentation from garbage slurry using the membrane free bioelectrochemical system». In: *Journal of Bioscience and Bioengineering* 114.1 (2012), pp. 64–69. ISSN: 1389-1723. DOI: https://doi.org/10.1016/j.jbiosc.2012.02.028. URL: https://www.sciencedirect.com/science/article/pii/S1389172312001077 (cit. on p. 5).

[7] Peter Clauwaert and Willy Verstraete. «Methanogenesis in membraneless microbial electrolysis cells». In: *Applied microbiology and biotechnology* 82.5 (2009), pp. 829–836 (cit. on pp. 5, 14).

[8] Mayur B. Kurade, Shouvik Saha, El-Sayed Salama, Swapnil M. Patil, Sanjay P. Govindwar, and Byong-Hun Jeon. «Acetoclastic methanogenesis led by Methanosarcina in anaerobic co-digestion of fats, oil and grease for enhanced production of methane». In: *Bioresource Technology* 272 (2019), pp. 351–359. ISSN: 0960-8524. DOI: https://doi.org/10.1016/j.biortech.2018.10.047. URL: https://www.sciencedirect.com/science/article/pii/S0960852418314780 (cit. on p. 6).

[9] Courtney Mobilian and Christopher B. Craft. «Wetland Soils: Physical and Chemical Properties and Biogeochemical Processes». In: *Encyclopedia of Inland Waters (Second Edition)*. Ed. by Thomas Mehner and Klement Tockner. Second Edition. Oxford: Elsevier, 2022, pp. 157–168. ISBN: 978-0-12-822041-2. DOI: https://doi.org/10.1016/B978-0-12-819166-8.00049-9. URL: https://www.sciencedirect.com/science/article/pii/B9780128191668000499 (cit. on p. 6).

[10] Mieke CAA Van Eerten-Jansen, Annemiek Ter Heijne, Cees JN Buisman, and Hubertus VM Hamelers. «Microbial electrolysis cells for production of methane from CO2: long-term performance and perspectives». In: *International Journal of Energy Research* 36.6 (2012), pp. 809–819 (cit. on pp. 7–9, 15).

[11] S.K. Bhattacharya, V. Uberoi, and M.M. Dronamraju. «Interaction between acetate fed sulfate reducers and methanogens». In: *Water Research* 30.10 (1996), pp. 2239–2246. ISSN: 0043-1354. DOI: https://doi.org/10.1016/0043-1354(95)00238-3. URL: https://www.sciencedirect.com/science/article/pii/0043135495002383 (cit. on p. 8).

[12] Michael Siegert, Xiu-Fen Li, Matthew D. Yates1, and Bruce E. Logan. «The presence of hydrogenotrophic methanogens in the inoculum improves methane gas production in microbial electrolysis cells». In: *Frontiers in Microbiology* 5 (Jan. 2015). DOI: 10.3389/fmicb.2014.00778 (cit. on pp. 8, 9).

[13] B. Sundén. *Hydrogen, Batteries and Fuel Cells*. Elsevier Science, 2019. ISBN: 9780128169513. URL: https://books.google.it/books?id=eCugDwAAQBAJ (cit. on pp. 10, 61).

[14] Inc. ANSYS. *ANSYS FLUENT 12.0 Fuel Cell Modules Manual*. English. Version 12.0. ANSYS, Inc. (cit. on pp. 10, 11).

[15] Sarzamin Khan and Jawad Ali. «2 - Chemical analysis of air and water». In: *Bioassays*. Ed. by Donat-P. Häder and Gilmar S. Erzinger. Elsevier, 2018, pp. 21–39. ISBN: 978-0-12-811861-0. DOI: https://doi.org/10.1016/B978-0-12-811861-0.00002-4. URL: https://www.sciencedirect.com/science/article/pii/B9780128118610000024 (cit. on p. 12).

[16] Matia Mainardis. *What is the chemical oxygen demand (COD) equivalent of short chain fatty acid (SCFA) and long chain fatty acid (LCFA)?* URL: https://www.researchgate.net/post/What_is_the_chemical_oxygen_demand_COD_equivalent_of_short_chain_fatty_acid_SCFA_and_long_chain_fatty_acid_LCFA (cit. on p. 13).

[17] Thangavel Sangeetha, Zechong Guo, Wenzong Liu, Minhua Cui, Chunxue Yang, Ling Wang, and Aijie Wang. «Cathode material as an influencing factor on beer wastewater treatment and methane production in a novel integrated upflow microbial electrolysis cell (Upflow-MEC)». In: *International Journal of Hydrogen Energy* 41.4 (2016), pp. 2189–2196. ISSN: 0360-3199.

DOI: https://doi.org/10.1016/j.ijhydene.2015.11.111. URL: https://www.sciencedirect.com/science/article/pii/S0360319915310880 (cit. on pp. 15, 17).

[18] Nabin Aryal, Yifeng Zhang, Suman Bajracharya, Deepak Pant, and Xuyuan Chen. «Microbial electrochemical approaches of carbon dioxide utilization for biogas upgrading». In: *Chemosphere* 291 (2022), p. 132843. ISSN: 0045-6535. DOI: https://doi.org/10.1016/j.chemosphere.2021.132843. URL: https://www.sciencedirect.com/science/article/pii/S0045653521033154 (cit. on p. 16).

[19] L. Gil-Carrera. «Municipal Wastewater Treatment in Microbial Electrolysis Cells». MA thesis. Universidad de León, 2014 (cit. on p. 16).

[20] Edouard Boujo. *Lecture notes in Numerical Flow Simulation*. Fall 2021 (cit. on pp. 18, 20, 23).

[21] Inc. ANSYS. *ANSYS FLUENT 12.0 Theory Guide*. English. Version 12.0. ANSYS, Inc. URL: https://www.afs.enea.it/project/neptunius/docs/fluent/html/th/main_pre.htm (cit. on pp. 20, 21, 51, 58–60, 62, 66–68, 70–72, 74).

[22] Mike Kuron. *3 Criteria for Assessing CFD Convergence*. 2015. URL: https://www.engineering.com/story/3-criteria-for-assessing-cfd-convergence (cit. on p. 22).

[23] John W. Slater. *NPARC Alliance CFD Verification and Validation: Validation Assessment*. 2021. URL: https://www.grc.nasa.gov/www/wind/valid/tutorial/valassess.html (cit. on p. 25).

[24] Dassault Systèmes. *SolidWorks 3D CAD*. Version 2019 SP1. Vélizy-Villacoublay, France: Dassault Systèmes. URL: https://www.3ds.com/products-services/solidworks/ (cit. on pp. 27, 40).

[25] LTD. SHANGHAI SONGHAN PLASTIC TECHNOLOGY CO. *Zoltek Panex 35® 50k Continuous Tow Commercial Carbon Fiber for Industrial Applications*. URL: http://www.lookpolymers.com/polymer_Zoltek-Panex-35-50k-

Continuous-Tow-Commercial-Carbon-Fiber-for-Industrial-Applications.php (cit. on p. 29).

[26] Daniel Chaparro. *A Comparison of ANSYS Fluent Meshing and Ansys Meshing for CFD*. 2021. URL: https://www.padtinc.com/2021/05/11/comparison-ansys-fluent-meshing-ansys-meshing-cfd/ (cit. on p. 44).

[27] cfd.ninja. *Ansys Meshing – Multizone + Inflation*. 2020. URL: https://cfd.ninja/ansys-meshing/ansys-meshing-multizone-inflation/ (cit. on p. 44).

[28] Mohammed El Ibrahimi, Ismail Khay, Anas El Maakoul, and Mohamed Bakhouya. «Food waste treatment through anaerobic co-digestion: Effects of mixing intensity on the thermohydraulic performance and methane production of a liquid recirculation digester». In: *Process Safety and Environmental Protection* 147 (2021), pp. 1171–1184. ISSN: 0957-5820. DOI: https://doi.org/10.1016/j.psep.2021.01.027. URL: https://www.sciencedirect.com/science/article/pii/S0957582021000367 (cit. on pp. 44, 47, 95).

[29] A.D. Le and Biao Zhou. «A general model of proton exchange membrane fuel cell». In: *Journal of Power Sources* 182 (2008), pp. 197–222 (cit. on pp. 54, 60–64, 83).

[30] Engineering ToolBox. *Water - Density, Specific Weight and Thermal Expansion Coefficients*. 2003. URL: https://www.engineeringtoolbox.com/water-density-specific-weight-d_595.html (cit. on p. 55).

[31] Engineering ToolBox. *Methane - Density and Specific Weight vs. Temperature and Pressure*. 2018. URL: https://www.engineeringtoolbox.com/methane-density-specific-weight-temperature-pressure-d_2020.html (cit. on p. 55).

[32] Kenneth Alambra. *Water Viscosity Calculator*. 2022. URL: https://www.omnicalculator.com/physics/water-viscosity (cit. on p. 55).

[33] Engineering ToolBox. *Methane - Dynamic and Kinematic Viscosity vs. Temperature and Pressure*. 2018. URL: https://www.engineeringtoolbox.com/methane-dynamic-kinematic-viscosity-temperature-pressure-d_2068.html (cit. on p. 55).

[34] Thermtest Europe AB. *Thermal Conductivity of Water*. 2021. URL: https://thermtest.se/thermal-conductivity-of-water (cit. on p. 55).

[35] Nuclear Power. *Methane – Density – Heat Capacity – Thermal Conductivity*. 2022. URL: https://material-properties.org/methane-density-heat-capacity-thermal-conductivity/ (cit. on p. 55).

[36] R Parsons. «The transfer coefficient in electrode reactions». In: *Croatica Chemica Acta* 42.2 (1970), pp. 281–291 (cit. on p. 55).

[37] P.S. Liu and G.F. Chen. «Chapter Nine - Characterization Methods: Basic Factors». In: *Porous Materials*. Ed. by P.S. Liu and G.F. Chen. Boston: Butterworth-Heinemann, 2014, pp. 411–492. ISBN: 978-0-12-407788-1. DOI: https://doi.org/10.1016/B978-0-12-407788-1.00009-5. URL: https://www.sciencedirect.com/science/article/pii/B9780124077881000095 (cit. on p. 56).

[38] Bruce Logan, Shaoan Cheng, Valerie Watson, and Garett Estadt. «Graphite Fiber Brush Anodes for Increased Power Production in Air-Cathode Microbial Fuel Cells». In: *Environmental Science & Technology* 41.9 (2007). PMID: 17539547, pp. 3341–3346. DOI: 10.1021/es062644y. URL: https://doi.org/10.1021/es062644y (cit. on pp. 56, 57).

[39] Fang Zhang, Matthew D. Merrill, Justin C. Tokash, Tomonori Saito, Shaoan Cheng, Michael A. Hickner, and Bruce E. Logan. «Mesh optimization for microbial fuel cell cathodes constructed around stainless steel mesh current collectors». In: *Journal of Power Sources* 196.3 (2011), pp. 1097–1102. ISSN: 0378-7753. DOI: https://doi.org/10.1016/j.jpowsour.2010.08.011. URL: https://www.sciencedirect.com/science/article/pii/S0378775310013297 (cit. on pp. 56, 57).

[40] Richard P. Wool. «13 - HURRICANE-RESISTANT HOUSES FROM SOYBEAN OIL AND NATURAL FIBERS». In: *Bio-Based Polymers and Composites*. Ed. by Richard P. Wool and Xiuzhi Susan Sun. Burlington: Academic Press, 2005, pp. 448–482. ISBN: 978-0-12-763952-9. DOI: https://doi.org/10.1016/B978-012763952-9/50014-9. URL: https://www.sciencedirect.com/science/article/pii/B9780127639529500149 (cit. on p. 57).

[41] Per Fidjestøl and Robert Lewis. «12 - Microsilica as an Addition». In: *Lea's Chemistry of Cement and Concrete (Fourth Edition)*. Ed. by Peter C. Hewlett. Fourth Edition. Oxford: Butterworth-Heinemann, 1998, pp. 679–712. ISBN: 978-0-7506-6256-7. DOI: https://doi.org/10.1016/B978-075066256-7/50024-2. URL: https://www.sciencedirect.com/science/article/pii/B9780750662567500242 (cit. on p. 57).

[42] C.O.Yadav, U.V.Joshi, and L.N.Patel. «CFD assisted Prediction of Hydrodynamic Parameters for Regenerator of Cryocooler». In: *Procedia Technology* 14 (2014), pp. 328–335 (cit. on pp. 57, 59).

[43] Hassan Ali Ozgoli and Saeed Elyasi. «A transient model of vanadium redox flow battery». In: *Mechanics  Industry* 17 (May 2016), p. 406. DOI: 10.1051/meca/2015065 (cit. on pp. 57, 58).

[44] ZOLTEK Corporation - Toray Group. *Commercial Carbon Fiber - ZOLTEK PX35*. 2022. URL: https://zoltek.com/products/px35/ (cit. on p. 57).

[45] thyssenkrupp Materials (UK) Ltd. *Stainless Steel 304 1.4301*. 2022. URL: https://www.thyssenkrupp-materials.co.uk/stainless-steel-304-14301.html (cit. on p. 57).

[46] Nadav Amdursky, Yiyang Lin, Noora Aho, and Gerrit Groenhof. «Exploring fast proton transfer events associated with lateral proton diffusion on the surface of membranes». In: *Proceedings of the National Academy of Sciences* 116.7 (2019), pp. 2443–2451. DOI: 10.1073/pnas.1812351116. eprint: https://www.pnas.org/doi/pdf/10.1073/pnas.1812351116. URL: https://www.pnas.org/doi/abs/10.1073/pnas.1812351116 (cit. on p. 58).

[47] Engineering ToolBox. *Gases Solved in Water - Diffusion Coefficients*. 2008. URL: https://www.engineeringtoolbox.com/diffusion-coefficients-d_1404.html (cit. on p. 61).

[48] Kyle B. Delwiche and Harold F. Hemond. «Methane Bubble Size Distributions, Flux, and Dissolution in a Freshwater Lake». In: *Environmental Science & Technology* 51.23 (2017). PMID: 29116771, pp. 13733–13739. DOI: 10.1021/acs.est.7b04243. eprint: https://doi.org/10.1021/acs.est.7b04243. URL: https://doi.org/10.1021/acs.est.7b04243 (cit. on p. 65).

[49] M. Pourtousi, P. Ganesan, Amin Kazemzadeh, Shanti C. Sandaran, and J.N. Sahu. «Methane bubble formation and dynamics in a rectangular bubble column: A CFD study». In: *Chemometrics and Intelligent Laboratory Systems* 147 (2015), pp. 111–120. ISSN: 0169-7439. DOI: https://doi.org/10.1016/j.chemolab.2015.08.003. URL: https://www.sciencedirect.com/science/article/pii/S016974391500194X (cit. on p. 65).

[50] Inc. ANSYS. *ANSYS FLUENT 12.0 User's Guide*. English. Version 12.0. ANSYS, Inc. (cit. on p. 65).

[51] Mikko Manninen, Veikko Taivassalo, and Sirpa Kallio. «On the mixture model for multiphase flow». In: (1996) (cit. on p. 66).

[52] Inc. ANSYS. *ANSYS FLUENT 12.0 Theory Guide*. English. Version 12.0. ANSYS, Inc. URL: https://www.afs.enea.it/project/neptunius/docs/fluent/html/th/node320.htm (cit. on p. 67).

[53] Inc. ANSYS. *ANSYS FLUENT 12.0 Theory Guide*. English. Version 12.0. ANSYS, Inc. URL: https://www.afs.enea.it/project/neptunius/docs/fluent/html/th/node294.htm (cit. on p. 68).

[54] Inc. ANSYS. *ANSYS FLUENT 12.0 Theory Guide*. English. Version 12.0. ANSYS, Inc. URL: https://www.afs.enea.it/project/neptunius/docs/fluent/html/th/node294.htm (cit. on pp. 68, 69).

[55] Inc. ANSYS. *ANSYS FLUENT 12.0 Theory Guide*. English. Version 12.0. ANSYS, Inc. URL: https://www.afs.enea.it/project/neptunius/docs/fluent/html/ug/node785.htm (cit. on p. 71).

[56] Inc. ANSYS. *ANSYS FLUENT 12.0 Theory Guide*. English. Version 12.0. ANSYS, Inc. URL: https://www.afs.enea.it/project/neptunius/docs/fluent/html/th/node373.htm (cit. on p. 72).

[57] Krishna Zore, Mohammad Azab, Balasubramanyam Sasanapuri, Shoaib Shah, and John Stokes. «ANSYS scale resolving simulations of launch-vehicle configuration at transonic speeds». In: *21th Annual CFD Symposium*. 2019, pp. 8–9 (cit. on p. 72).

[58] *CFD Numerics: Relaxation Factors*. URL: https://www.simscale.com/docs/simulation-setup/numerics/relaxation-factors/ (cit. on p. 73).